

A NOVEL DAMAGE INDEX FOR FATIGUE DAMAGE DETECTION  
IN A LAMINATED COMPOSITES  
USING LAMB WAVES

by

DAIGO SEKI

SAMIT ROY, COMMITTEE CHAIR  
MARK E. BARKEY  
WEI SONG

A THESIS

Submitted in partial fulfillment of the requirements  
for the degree of Master of Science in the Department  
of Aerospace Engineering and Mechanics  
in the Graduate School of  
The University of Alabama

TUSCALOOSA, ALABAMA

2015

Copyright Daigo Seki 2015  
ALL RIGHTS RESERVED

## ABSTRACT

A well-established structural health monitoring (SHM) technique, the Lamb wave based approach, is used for fatigue damage identification in a laminated composite. A novel damage index, 'normalized correlation moment' (NCM) which is composed of the nth moment of the cross correlation of the baseline and comparison waves, was used as damage index for monitoring damage in composites and compared with the signal difference coefficient (SDC) which is one of the most commonly used damage indices. Composite specimens were fabricated by the hand layup method by followed by compression. Piezo electric disks mounted on composite specimens were used as actuators and sensors. Three point bending fatigue tests were carried out on an intact composite laminate and a delaminated composite laminate with  $[0_6/90_4/0_6]$  orientation. Finite element analysis was performed to test the validity of SDC and NCM for fatigue damage.

## **LIST OF ABBREVIATIONS AND SYMBOLS**

AE	Acoustic emission
AHM	Boeing airplane health management
CBM	Condition-based maintenance
CFRP	Carbon fiber reinforced plastic
DAQ	Data acquisition
DI	Damage index
EMM	Equivalent matrix method
FBG	Fiber Bragg grating
GAs	Genetic algorithms
GMM	Global matrix method
LISA	Local interaction simulation approach
MFC	Macro fiber composite
NCM	Normalized correlation moment
NDE	Nondestructive evaluation
NDI	Nondestructive inspection
PZT	Lead zirconate titanate
RTM	Resin transfer molding
SAFE	Semi-analytical finite element method
SDC	Signal difference coefficient

SHM	Structural health monitoring
TBM	Time-based maintenance
TMM	Transfer matrix method
ToF	Time of flight
VARTM	Vacuum assisted resin transfer molding
3D	Three dimensional

## **ACKNOWLEDGMENTS**

I would like to express my high appreciation to Dr. Samit Roy, my adviser, for his advice, kindness, and encouragement. Without his support, this work would have never finished. I would like to express my sincere gratitude to my thesis committee members, Dr. Mark E. Barkey and Dr. Wei Song for their time and valuable feedback. I am indebted to Dr. Mark E. Barkey for his support and help with conducting fatigue test. The fatigue test would not have been finished without his help. I also would like to thank my research members, Shahab Torkamani, Avinash Reddy Akepati, Abhisheck Kumar, Shibo Li, Pruthul Ravindranath, and Ankit Srivastav for their support, technical discussion, and valuable advice. I would like to thank my family and my friends in U.S and Japan for their spiritual support and encouragement. Finally, I would like to express my great appreciation to my girlfriend, Kazuki Okushi. Without her support, I could not have had great and precious experience in the U.S.

## CONTENTS

ABSTRACT.....	ii
LIST OF ABBREVIATIONS AND SYMBOLS .....	iii
ACKNOWLEDGMENTS .....	v
LIST OF TABLES .....	viii
LIST OF FIGURES .....	ix
CHAPTER 1 INTRODUCTION .....	1
CHAPTER 2 LITERATURE REVIEW.....	8
2.1 Introduction to Lamb waves.....	8
2.2 Damage detection using Lamb waves .....	12
2.3 Damage identification algorithms .....	13
2.4 Fatigue damage .....	18
2.5 Finite element analysis.....	18
CHAPTER 3 EXPERIMENTAL ANALYSIS .....	20
3.1 Fabrication of composite specimens .....	20
3.2 Data acquisition setup .....	23
3.3.1 Experimental setup.....	25
3.4 Experimental results.....	26

CHAPTER 4 SIMULATION ANALYSIS.....	29
4.1 Composite and delamination modeling benchmark test .....	29
4.2 Lamb wave propagation test .....	32
4.3 Fatigue damage detection using Lamb wave .....	35
4.3.1 Models with reduced material properties.....	35
4.3.2 Models with reduced material properties and increasing size of damage.....	40
CHAPTER 5 RESULTS AND DISCUSSION .....	45
5.1 Comparison of experimental and simulation results .....	45
5.2 Validity of the NCM damage index for fatigue damage .....	51
CHAPTER 6 CONCLUSIONS AND FUTURE WORK.....	54
6.1 Conclusions .....	54
6.2 Future work .....	55
REFERENCES .....	57
APPENDIX A: LabVIEW program.....	62
APPENDIX B: MATLAB program .....	64

## LIST OF TABLES

Table 4.1 Material properties of IM7-8552.....	30
Table 4.2 Comparison of beam theory and simulation results.....	31
Table 4.3 SDC and NCM for undamaged and damaged model.....	34
Table 4.4 Material properties of IM7-8552 using micromechanics.....	35
Table 4.5 SDC and NCM for three comparison cases: Undamaged-90% properties, Undamaged-80% properties, and Undamaged-70% properties .....	37
Table 4.6 SDC and NCM for three comparison cases: Damaged-90% properties, Damaged-80% properties, and Damaged-70% properties.....	39
Table 4.7 SDC and NCM for six cases: Undamaged-0.254 <i>mm</i> , Undamaged-0.127 <i>mm</i> , Undamaged-5.08 <i>mm</i> , Undamaged-7.62 <i>mm</i> , and Undamaged-10.16 <i>mm</i> .....	42
Table 4.8 SDC and NCM for six cases: Damaged-0.254 <i>mm</i> , Damaged-0.127 <i>mm</i> , Damaged-5.08 <i>mm</i> , Damaged-7.62 <i>mm</i> , and Damaged-10.16 <i>mm</i> .....	44
Table 5.1 Material properties of IM7-SC780.....	45
Table 5.2 Delamination growth for three specimens observed in the experiment.....	48

## LIST OF FIGURES

Figure 1.1 Application of advanced composite material in the Boeing787 dreamliner [1].....	1
Figure 1.2 (a) image of impacted composites surface (b) ultrasonic inspection result [2].....	2
Figure 1.3 Crash of Japan Airlines Flight 123 [3] .....	3
Figure 1.4 Collapse of the Seongsu Bridge in Korea [4].....	3
Figure 2.1 Lowest order symmetric modes and anti-symmetric modes of Lamb waves .....	9
Figure 2.2 Lamb wave dispersion curves for an aluminum plate.....	10
Figure 2.3 Dispersion curves for the composite laminate with $[0_6/90_4/0_6]$ orientations.....	11
Figure 2.4 Pitch-catch configuration.....	13
Figure 2.5 Pulse-echo configuration.....	13
Figure 2.6 Sensitivity of SDC and NCM to wave attenuation and increase.....	16
Figure 2.7 Sensitivity of SDC and NCM to time of flight.....	17
Figure 3.1 Schematic view of simulated delamination.....	21
Figure 3.2 Surface mold.....	21
Figure 3.3 Composite specimens .....	22
Figure 3.4 Schematic view of data acquisition set up.....	23
Figure 3.5 Test specimen with three PZTs .....	24
Figure 3.6 Tone burst having 5 cycles with a center frequency of 50 kHz.....	25
Figure 3.7 Schematic view of experimental setup .....	26
Figure 3.8 Stiffness degradation for three damaged specimens .....	27

Figure 3.9 NCM for three damaged specimens .....	27
Figure 3.10 SDC for three damaged specimens.....	28
Figure 4.1 Composite cantilever beam subjected to a resultant shear load 1 N at its end.....	29
Figure 4.2 Dimensions of the composite cantilever beam with $[0/90_2/0]$ orientations.....	30
Figure 4.3 2mm length delamination at the mid span of the beam between 2th and 3th layer	30
Figure 4.4 Dimensions of the composite laminate with $[0_6/90_4/0_6]$ orientations.....	33
Figure 4.5 Boundary conditions of the composite laminate model .....	33
Figure 4.6 Location of actuators and three sensors on top surface.....	33
Figure 4.7 Pure excitation.....	34
Figure 4.8 Response from the No.2 sensor for both undamaged and damaged model.....	34
Figure 4.9 Response from the No.2 snesor for the undamaged model, with 90% properties, with 80% properties, and with 70% properties. ....	36
Figure 4.10 SDC and NCM (n=2) for three comparison cases: Undamaged-90% properties, Undamaged-80% properties, and Undamaged-70% properties.....	37
Figure 4.11 Response from the No.2 snesor for the damaged model, with 90% properties, with 80% properties, and with 70% properties. ....	38
Figure 4.12 SDC and NCM (n=2) for three comparison cases: Damaged-90% properties, Undamaged-80% properties, and Undamaged-70% properties.....	39
Figure 4.13 Schematic view of undamaged and damaged models with reduced material properties and increasing size of damage .....	40
Figure 4.14 Responses from No.2 sensor for undamaged model with 90% material properties, with 0.254 mm damage, with 1.27 mm damage, with 2.54 mm damage, with 5.08 mm damage, with 7.62 mm damage, and with 10.16 mm damage .....	41
Figure 4.15 SDC and NCM (n=2) for six cases: Undamaged-0.254 mm, Undamaged-0.127 mm, Undamaged-5.08 mm, Undamaged-7.62 mm, and Undamaged-10.16 mm .....	41
Figure 4.16 Responses from No.2 sensors for damaged model with 90% material properties, with 0.254 mm damage, with 1.27 mm damage, with 2.54 mm damage, with 5.08 mm damage, with 7.62 mm damage, and with 10.16 mm damage .....	43

Figure 4.17 SDC and NCM (n=2) for six cases: Damaged-0.254 mm, Damaged-0.127 mm, Damaged-5.08 mm, Damaged-7.62 mm, and Damaged-10.16 mm .....	43
Figure 5.1 Prefabroccated 50.8 mm (2 inch) length delamination .....	46
Figure 5.2 Side view of specimen showing boundary conditions of the FEA model for comparison with experimental results .....	46
Figure 5.3 Delamination growth for three specimens observed in the experiment .....	47
Figure 5.4 Delamination growth at 23500 cycles for damaged specimen-2.....	48
Figure 5.5 Simulating delamination growth in the FEA model .....	49
Figure 5.6 SDC for comparison of the experiment and the simulation .....	49
Figure 5.7 NCM for comparison of the experiment and the simulation.....	50
Figure 5.8 Sensitivity of NCM to tiem of flight and wave attenuation .....	52
Figure 5.9 Sensitivity of NCM to time of flight and wave amplitude increase .....	52
Figure 5.10 Received signals at 0 cycles and 500 cycles in the experiment .....	53
Figure 6.1 Temperature increase of MFC .....	56

# CHAPTER 1

## INTRODUCTION

Structures such as a car, an airplane, a sporting equipment, a ship, a fuel tank, a satellite, a bicycle, and a train have been made of carbon fiber reinforced plastic (CFRP) over the past few decades. For example, the Boeing 787 contains almost 50% composites of its total weight in carbon composites as shown in Figure 1.1 [1]. The reason why CFRP is often used for primary airframe structures is because of its high specific stiffness and strength ratio, tailor ability, light-weight, good corrosion resistance and radar absorption, and ease of manufacturing.

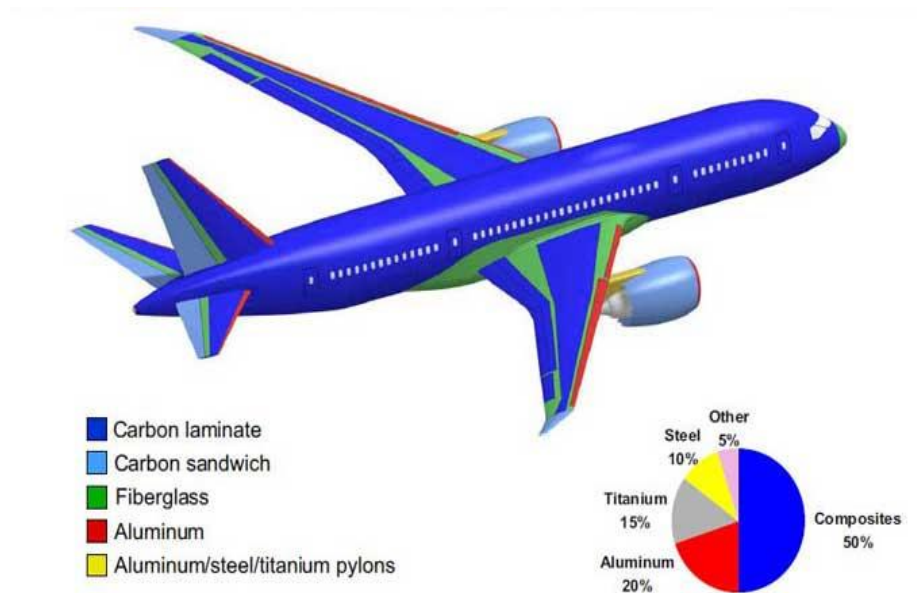


Figure 1.1 Application of advanced composite material in the Boeing787 dreamliner [1]

However, composite materials are susceptible to damage from impact, fatigue loading, and hygrothermal effect. Mechanisms of damage in CFRP such as delamination, matrix cracking, fiber buckling, fiber break age, and fiber matrix debonding are more complicated than metals. The damage directly impacts the safety of structures. For instance, impact damage makes the compression strength of composite dramatically decrease although impact damage is barely visible as shown in Figure 1.2 [2]. Therefore, damage detection in the early life cycle is very important to ensure the reliability of structures.

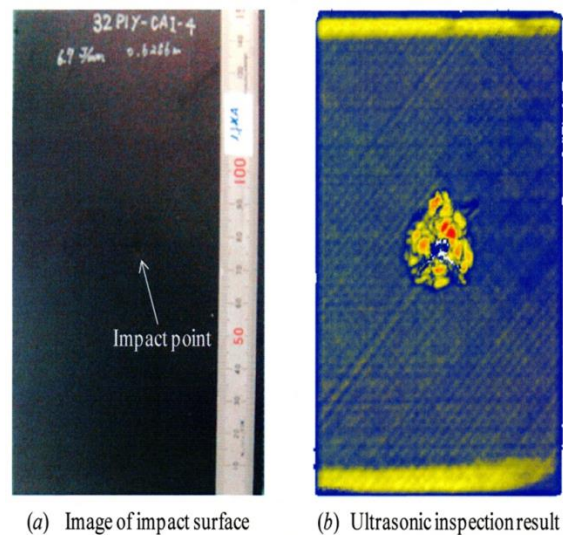


Figure 1.2 (a) image of impacted composites surface (b) ultrasonic inspection result [2]

Some techniques for damage detection have been investigated because several catastrophic accidents have occurred: The crash of Japan Airlines Flight 123 which is the deadliest single aircraft accident in history [3] shown in Figure 1.3, the metal fatigue on British Overseas Airways Corporation Flight 781, the collapse of the Seongsu Bridge in Korea [4] shown in Figure 1.4, the derailment of Intercity-Express (ICE) in German, and the Space Shuttle Columbia disaster. Most of these accidents are caused because of fatigue damage.



Figure 1.3 Crash of Japan Airlines Flight 123 [3]



Figure 1.4 Collapse of the Seongsu Bridge in Korea [4]

The main cause of the crash of Japan Airlines Flight 123 was an improper repair. The improper repair resulted in allowing fatigue crack to propagate rapidly causing rapid break-up of the fuselage aft bulkhead. The collapse of the Seongsu Bridge in Korea was caused by improper welding of the steel trusses of the suspension structure beneath the concrete slab roadway [4] and metal fatigue occurred earlier than expected. Most of these accidents were caused by human error leading to fatigue failure. Therefore, non-destructive evaluation (NDE) techniques such as

ultrasonic scanning, X-ray CT scanning, magnetic resonance imagery, and acoustic holography, which are one of the techniques to investigate damage in structures, have been developed and researched. In NDE technique, in which sensors and actuators are usually external to the structure, damage can be detected at early stage in a non-destructive manner and thereby catastrophic events can be prevented. Traditionally, NDE is usually conducted at scheduled intervals. This means NDE technique cannot automatically provide the information of damage when structures are in service. That is because most NDE equipment we used cannot provide efficient access to appropriate sections of the structures during service [5].

Recent development of sensor technology allows us to continuously monitor the structures in real time. This technology is called Structural Health Monitoring (SHM) which evolved from NDE. Unlike in traditional NDE, in SHM sensors and actuators are continuously monitored on structures while they are in service and provide data for “repair/replace/ignore” decision process. Consequently, by utilizing the concept of “condition-based maintenance (CBM)” as opposed to “time-based maintenance (TBM)” SHM can reduce unnecessary maintenance and thereby, reduce the total maintenance cost. In addition, SHM can be used to predict the remaining useful life by detecting the damage size and location. Thus, SHM has been gaining popularity in aerospace engineering and civil engineering fields. For instance, SHM is used for monitoring bridges in Japan [6]. The Boeing Airplane Health Management (AHM) is on board Boeing 787 [7]. In general, SHM consists of four processes: (1) operational evaluation, (2) data acquisition, fusion, and cleansing, (3) feature extraction and information condensation, (4) and statistical model development for feature discrimination. Operational evaluation decides the economic and life safety motivations, damage types to be monitored, operational and environmental conditions, and the limitations of acquiring data under the operational

environment. Data acquisition decides the number of reading samples, the hardware for the acquisition, the storage, and the transmission of data, the type, the number, and the location of sensors. Feature extraction and information condensation involve the identification of damage-sensitive properties using the measured vibration response to differentiate between the undamaged and damaged structure. Statistical model development for feature discrimination is to decide the damage state: is there damage in the system? If so, where is the damage in the system? what kind of damage is present? how severe is the damage? and how much useful life remains? [8].

Damage detection is conducted by active or passive approaches. The active approach uses an actuator such as a lead zirconate titanate (PZT) and a macro fiber composite (MFC) and measure the responses. On the other hand, a passive approach does not use any actuators but sensors to receive the responses. Both approaches use mounted or embedded actuators/sensors to receive the responses [9]. Staszewski *et al.* [9] demonstrated both approaches for impact damage detection since detection of impact damage is an important problem in aerospace industries. Active approach based on Lamb wave responses and a 3-D laser vibrometer detected and estimated the location of damage and its severity, but this approach needed sophisticated instrumentation. Passive approach using Genetic Algorithms (GAs) found the location of damage although this method did not need any sophisticated instrumentation. Staszewski concluded a combination of both approaches may work well.

Global or local changes of a structure can be used for damage parameters. Usually, global changes including eigen-frequency, mode shape, strain energy, damping properties are not sensitive to damage before it reaches a noticeable size. Local changes that can be calibrated by electro-mechanical impedance and displacement or strain are sensitive when damage is near

sensors but they are insensitive to damage that is distant from sensors. Acoustic emission (AE) can measure damage size and location by triangulation and predict damage growth but this method cannot evaluate damage severity [5]. Recently, wave-based approaches have been researched and quantitatively evaluate damage [10-13].

Wave-based approaches have significant advantages: a wave propagates a long distance and is high sensitive to abnormalities and inhomogeneity in a structure. Over the past few decades, damage detection using Lamb waves have been established and favored by researchers because its advantages: low cost, capability of inspecting large structure with a few transducers and examining the entire cross-sectional area of structures to detect surface and internal defects, high sensitivity to manufacturing defects and in service damage, the possibility of inspecting coated or insulated structures such as underground pipelines, and use in automated damage detection [5]. Kessler *et al.* [10] presented Lamb wave methods for composite materials and concluded that Lamb wave techniques provided more information about damage presence and severity than frequency response techniques [11]. Nagabhushana *et al.* [12] also used Lamb wave to identify crack damage in composites. In this thesis, SHM using Lamb waves was conducted to detect fatigue damage in laminated CFRP composite materials. Fatigue delamination commonly occurs between adjacent composite layers in service time and because it remains hidden inside the laminate, it often causes catastrophic events. Therefore, detecting delamination fatigue damage at an early stage is critical. In this thesis, piezoelectric actuators mounted on the composite surface were used to generate Lamb waves and the responses were measured by piezoelectric sensors mounted on the composite surface. As a damage index, a signal difference coefficient (SDC) developed by researchers at Penn State University [13] and a

normalized correlation moment (NCM) developed by Torkamani [14] were used to evaluate damage. Finite element analysis was used to validate the experimental results

This thesis consists of six chapters. Chapter 2 provides the literature review including introduction to Lamb wave, damage identification based on Lamb wave technique, damage identification algorithm, fatigue damage, and finite element analysis for simulating Lamb wave propagation. Damage indices including SDC and NCM are also introduced in this chapter. Chapter 3 provides the experimental study to detect delamination fatigue damage including composite laminate fabrication with and without built-in delamination, data acquisition setup, experimental setup, and experimental results. Three point bending fatigue test was conducted and resulting damage indices, SDC and NCM, were calculated. Chapter 4 describes the finite element simulation analysis. ABAQUS, a commercial finite element code, was used for simulating Lamb wave propagation in a composite laminate. SDC and NCM were also calculated from the FEA data. Results and discussion are summarized in Chapter 5. Conclusions and recommendations for future works are presented in Chapter 6.

## CHAPTER 2

### LITERATURE REVIEW

This Chapter includes the introduction to Lamb waves, damage detection using Lamb waves, damage identification algorithms, fatigue damage, and finite element analysis.

#### 2.1 Introduction to Lamb waves

Lamb waves were first described as one of acoustic waves by Horace Lamb, English mathematician, in 1917 [15]. However, he did not use Lamb waves for damage detection. The first person to use Lamb waves for damage detection is Worlton [16] in 1961. Lamb waves are elastic waves: the wave propagates in an elastic plate-like structure, and can propagate long distances and can be used to detect internal and surface damage. Lamb waves have two fundamental modes, symmetric modes ( $S_i$ ,  $i = 0, 1, \dots$ ) and anti-symmetric modes ( $A_i$ ,  $i = 0, 1, \dots$ ). The lowest order symmetric modes ( $S_0$ ) and lowest order anti-symmetric modes ( $A_0$ ) are shown in Figure 2.1.  $S_i$  modes have in-plane motion of particles while  $A_i$  modes have out of plane motion of particles. Lamb waves have infinite modes, and as the frequency increases, higher modes are generated. Lamb waves are dispersive, which means their wave velocity depend on their frequency and plate thickness. For example, Lamb waves with a central frequency 300 kHz are excited in a plate like structure. The  $S_0$  mode peaks at 293 kHz and the  $A_0$  mode peaks at 332 kHz in the captured signal [5]. They are not equal to the original central frequency 300 kHz. This phenomenon is called dispersion and makes the received waves

complicated. Therefore, for damage detection, excited Lamb waves should be less dispersive and have only the required modes.

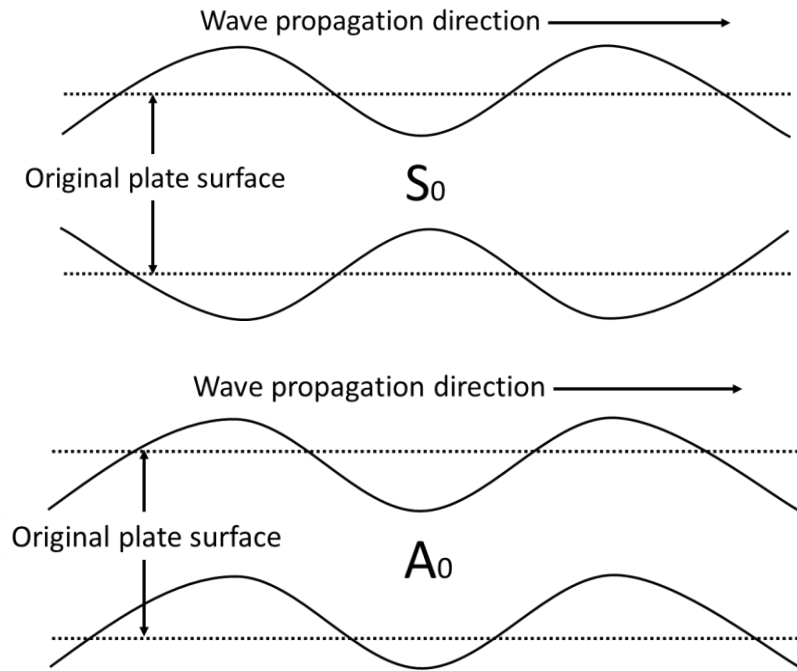


Figure 2.1 Lowest order symmetric modes and anti-symmetric modes of Lamb waves

In order to decide the frequency of Lamb wave for damage detection, dispersion curves are commonly used. The Rayleigh-Lamb equations can be used to determine dispersion curves for isotropic materials. As an example, dispersion curves of a 4mm thick aluminum plate determined numerically are shown in Figure 2.2. The first graph shows the relationship between the phase velocity and the frequency of Lamb wave. Similarly, the second graph shows the group velocity vs the frequency of Lamb wave [17]. Here, the phase velocity is the velocity of the wave of the particular frequency and the group velocity is the velocity of the overall wave packet. As the frequency increases, more modes exist. From the dispersion curves, the frequency of Lamb wave is chosen so that the Lamb wave is not dispersive and has a required mode. In the case of aluminum, 300 kHz Lamb wave can be chosen because it has only  $S_0$  mode and  $A_0$  mode. More details can be found in [17].

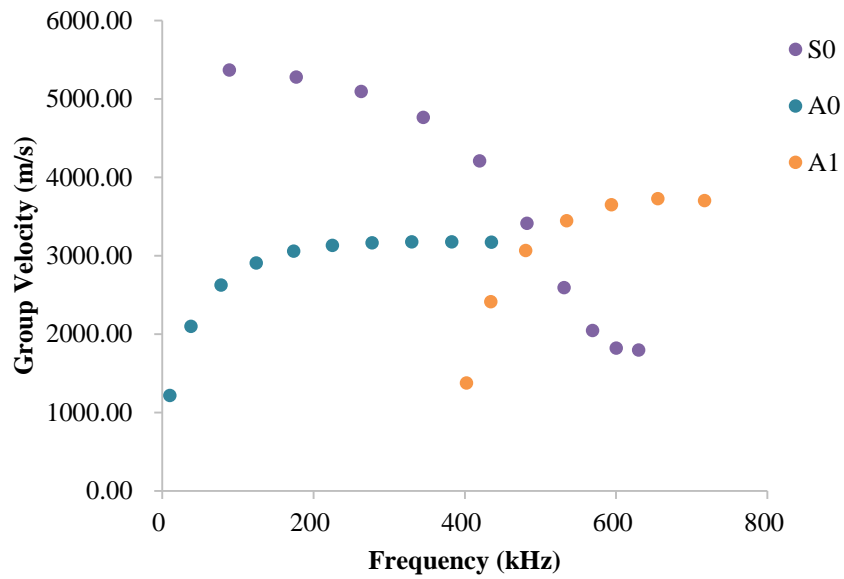
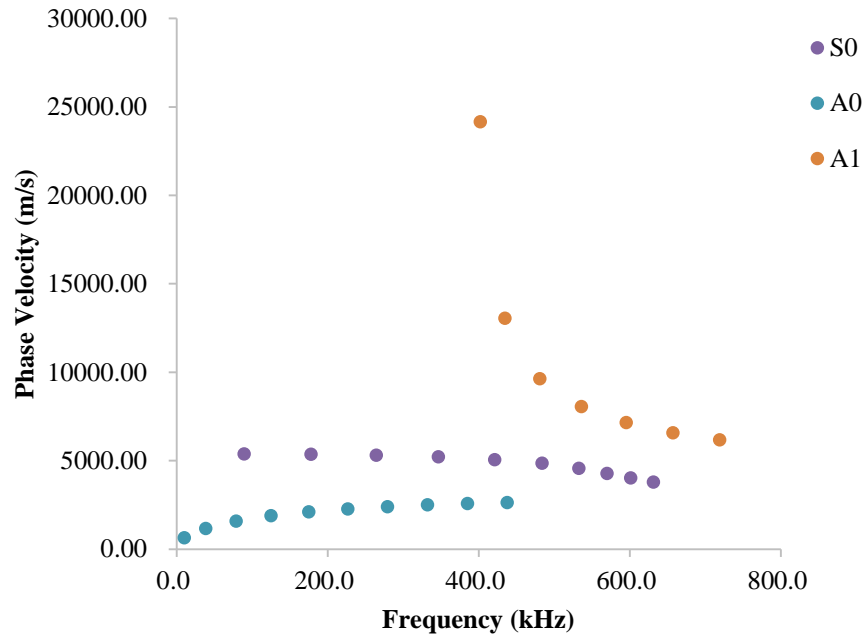


Figure 2.2 Lamb wave dispersion curves for an aluminum plate

Dispersion curves for anisotropic composite materials are more complex than those for isotropic metals. There are several methods to evaluate dispersion curves in composites: transfer matrix method (TMM) described in [18], global matrix method (GMM) developed by [19], semi-analytical finite element method (SAFE) studied in [20], local interaction simulation approach

(LISA) [21], and equivalent matrix method (EMM) used in [22]. These details are described in [23]. Finding dispersion curves of composites is not easy and commercial soft wares such as DISPERSE developed by Imperial College in London and GUIGUW [24] can be used. In this study, GUIGUW was used to detect dispersion curves for the composite laminate with  $[0_6/90_4/0_6]$  orientations.

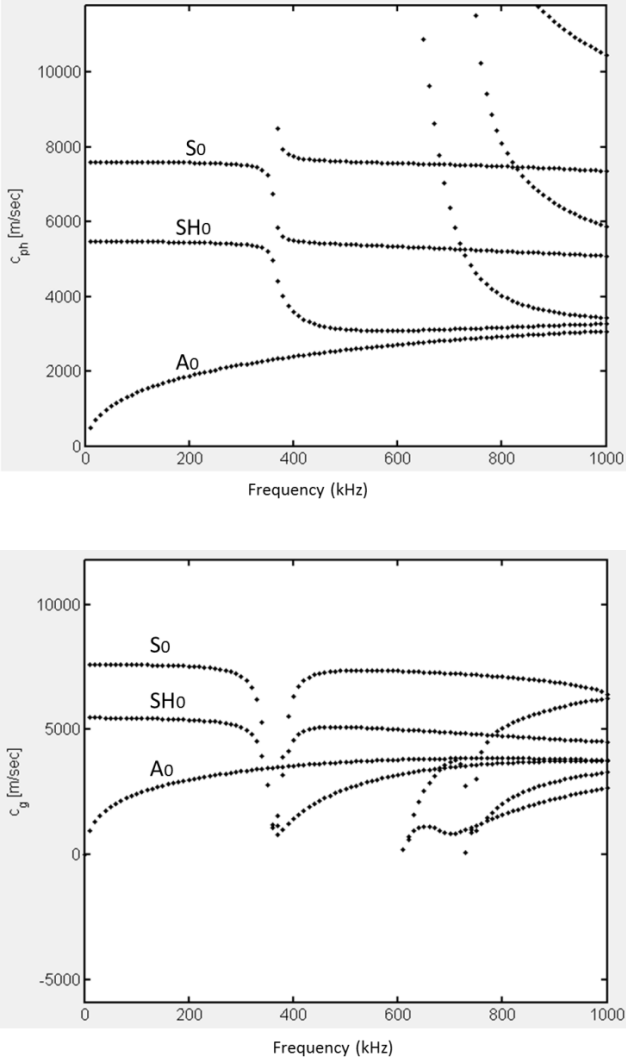


Figure 2.3 Dispersion curves for the composite laminate with  $[0_6/90_4/0_6]$  orientations

In Figure 2.3,  $C_{ph}$  and  $C_g$  are phase velocity and group velocity, respectively.  $SH_0$  is shear horizontal wave mode which dominates in-plane motion of particles but its direction is perpendicular of wave propagation.

## **2.2 Damage detection using Lamb waves**

Lamb waves have been used for damage detection and there are many studies for damage detection using Lamb waves [25-31], and two basic configurations, pitch-catch and pulse echo shown in Figure 2.4 and Figure 2.5. In a pitch-catch configuration, activated waves propagate across damage and are captured by another sensor. Damage can be found by comparing the changes between initial waves and transmitted waves. In a pulse-echo configuration, actuators and sensors are located at the same side and sensors capture the echoed wave from damage. This can detect the location of damage by the time of flight of the reflections. The time of flight (ToF) is one of the simple features of a Lamb wave for damage identification and is defined as the time lag between the incident wave that the sensor first captures and the echoed wave from damage that the same sensor subsequently captures. It is further described in section 6.2.2 in [5]. Diamanti and Soutis used ToF for damage location in [25].

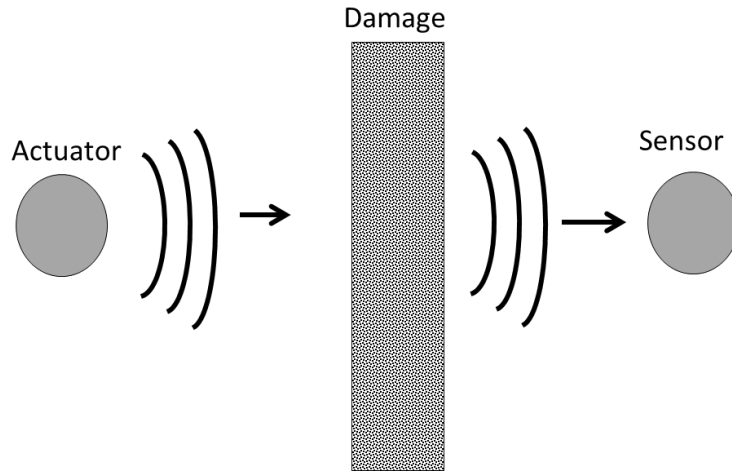


Figure 2.4 Pitch-catch configuration

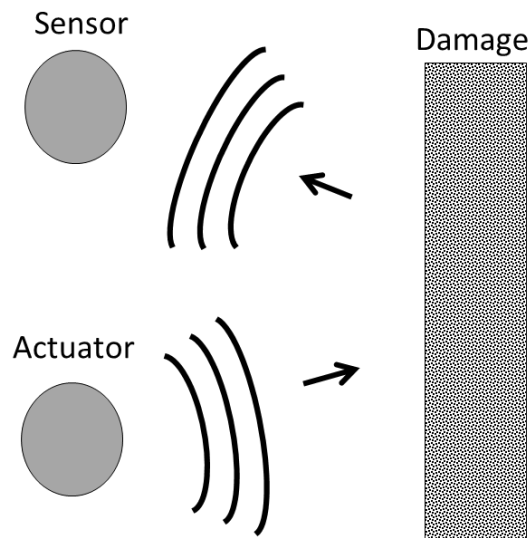


Figure 2.5 Pulse-echo configuration

### 2.3 Damage identification algorithms

In the wave based approach, detecting changes between the incident and the captured waveforms is very important to identify damage. Some damage identification algorithms have been used to find certain characteristics of the waveforms associated with those changes. Those characteristics of waveforms are referred as “features” and applying damage identification algorithms is referred as “feature extraction” [14]. As a feature extraction, two main approaches

exist: model-based feature extraction and signal-based feature extraction. Model-based feature extraction is suitable in applications where the user has knowledge of the loading and damage in advance. For example, the embedded sensitivity method is useful when the location of the damage is already known so that the proper measurement can be performed to qualify the damage level [26]. In the signal-based feature extraction, without using physical models, features of waveforms are directly extracted from signals. In this approach, an indicator of damage called damage index (DI) are often used. Three types of damage indices exist: DIs in time domain, DIs in frequency domain, and DIs in joint time/frequency domain. The simplest DI in time domain is comparing the peak amplitude between the baseline (undamaged) and the comparison (damaged) signal.

A damage index based on the Pearson correlation coefficient developed by researchers at Penn State University [13] is often used because this damage index can be applied for challenging problems in damage detection in composites. The Pearson correlation coefficient is a statistical feature and is defined by Equation (2.1).

$$\text{The Pearson correlation coefficient} = \frac{\text{Cov}(f_1(t), f_2(t))}{\sigma_{f_1} \sigma_{f_2}} \quad (2.1)$$

where  $f_1(t)$  and  $f_2(t)$  are the baseline and the comparison waveform,  $\text{Cov}(f_1(t), f_2(t))$  is the covariance of  $f_1(t)$  and  $f_2(t)$ , and  $\sigma_{f_1} \sigma_{f_2}$  is the product of the standard deviations of  $f_1(t)$  and  $f_2(t)$ . The damage index based on the Pearson correlation coefficient is defined by Equation (2.2) and is called the signal difference coefficient (SDC).

$$\text{SDC} = 1 - \left| \frac{\text{Cov}(f_1(t), f_2(t))}{\sigma_{f_1} \sigma_{f_2}} \right| \quad (2.2)$$

SDC statistically compares the present signal and the reference signal and indicates the overall change in the structure. SDC has been successful in the identification of damage in multiple

challenging cases. Gao *et al.* [13] applied SDC for an artificial defect in an aircraft wing. Although an aircraft component is generally a complicated shape structure, which makes captured waveforms complicated, SDC was able to identify the damage. Zhao *et al.* [27] used some tomography algorithms with SDC feature for the identification of corrosion on an aircraft wing and identified even small simulated corrosion defects. Yan *et al.* [28] used the damage identification algorithm based on SDC for an aluminum plate and a composite plate and their algorithm found the location, the size, and the severity of damage. Lissenden *et al.* [29] applied SDC for fatigue damage in laminated composite plates and SDC was able to provide an early indication of damage. Keulen *et al.* [30] compared their damage identification algorithm with SDC for verification. Thus, SDC has widely been used for damage identification.

A novel time domain damage index, called normalized correlation moment (NCM), was introduced by Torkamani *et al.* [14] and is based on cross-correlation and moment. In signal processing, cross-correlation is used for measuring the similarity between two signals. For example, when you want to detect where the specific signal is in a certain signal component, performing cross-correlation can detect it by measuring the similarity between the signal you want to find and the certain signal component. Cross-correlation of two signals,  $f_1(t)$  and  $f_2(t)$ , is given by Equation (2.3).

$$r_{f_1 f_2}(\tau) = \int_{-\infty}^{\infty} f_1(t) f_2(t - \tau) dt \quad (2.3)$$

where  $f_1(t)$  and  $f_2(t)$  are the baseline and the comparison waveform and  $\tau$  is referred to the lag parameter. This equation mathematically means calculating a series of shifted dot products. When two signals are most similar to each other in terms of frequency and phase, the cross-correlation takes maximum value. In damage detection, measuring changes of frequency and phase is important. In addition, wave attenuation is an important factor. Torkamani *et al.*

introduced the concept of moment to account for the overall shape of the waveform. Statistically speaking, a moment is able to measure the shape of a distribution. He took advantage of nth moment of cross-correlation, resulting in a novel damage index named normalized correlation moment (NCM) as given by Equation (2.4).

$$NCM = \frac{\int_0^T \tau^n |r_{f_1 f_2}(\tau)| d\tau - \int_0^T \tau^n |r_{f_1 f_1}(\tau)| d\tau}{\int_0^T \tau^n |r_{f_1 f_1}(\tau)| d\tau} \quad (2.4)$$

where  $r_{f_1 f_2}(\tau)$  is the cross-correlation of the baseline with the comparison waveform,  $r_{f_1 f_1}(\tau)$  is the cross-correlation of the baseline with itself, called autocorrelation,  $T$  is the duration of signal acquisition, and  $n$  is the order of the statistical moment. The moment order,  $n$ , is an arbitrary value. If the baseline and the comparison waveform are the same, NCM will be zero, which means there is no damage. In [14], Torkamani *et al.* showed some advantages of this damage index, NCM, as compared with SDC. The major advantage of NCM is its sensitivity to wave attenuation while SDC cannot effectively monitor wave attenuation.

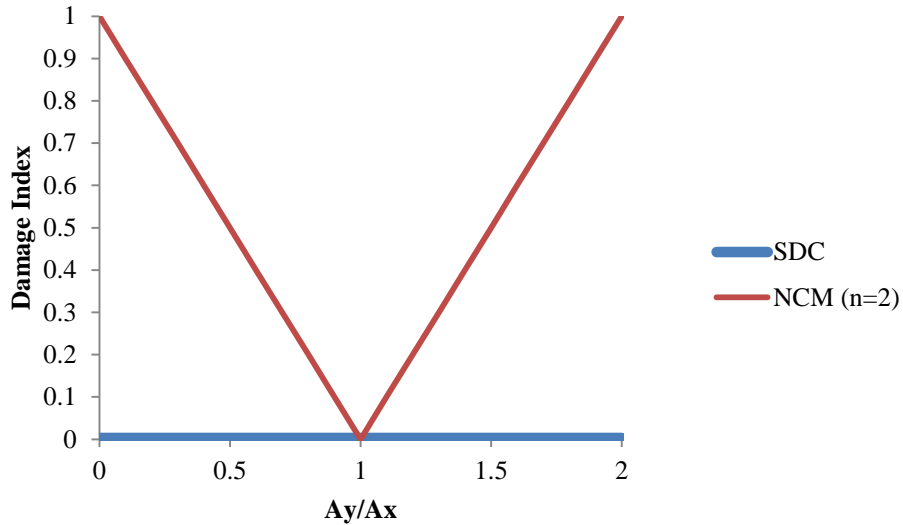


Figure 2.6 Sensitivity of SDC and NCM to wave attenuation and increase

In Figure 2.6, the amplitude of the comparison wave ( $A_y$ ) is changing from 0% to 200% of the baseline amplitude ( $A_x$ ). SDC is completely insensitive to wave attenuation and increase while NCM can evaluate wave attenuation and increase. In general, damage or in-homogeneities such as stiffeners or fasteners cause the wave attenuation [31]. Therefore, the capability of monitoring wave attenuation and increase is very significant advantage. NCM has other advantages: greater sensitivity to frequency difference, time of flight in Figure 2.7, and less susceptibility to noise. More detail is in [14].

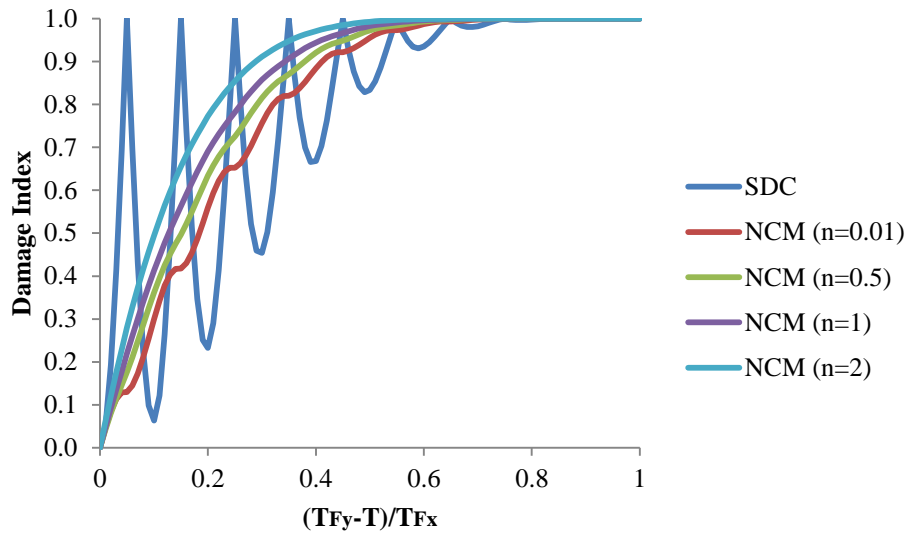


Figure 2.7 Sensitivity of SDC and NCM to time of flight

In Figure 2.7, the duration of the baseline signal is  $T_{Fx} = T$  and that of the signal of the comparison wave is increased from  $T_{Fy} = T$  to  $T_{Fy} = 2T$ . The amplitude of both signals is 1. SDC shows the oscillating sensitivity while NCM shows a monotonic sensitivity to time of flight. NCM showed distinct advantages for the identification of delamination in composite laminates compared with SDC. In this thesis, NCM is applied for fatigue damage and is compared with SDC.

## 2.4 Fatigue damage

As mentioned earlier, fatigue damage often leads to catastrophic events. In aerospace industry, traditional fatigue analysis has been conducted to predict the remaining fatigue life and when maintenance is necessary. However, fatigue damage in composites is much different from traditional metals often used in aerospace structures and is barely visible to outside observers. Fatigue damage in composites can also initiate earlier than in a metallic alloy depending on the type of loading. There are various publications regarding monitoring fatigue damage. Takeda *et al.* [32] used fiber Bragg grating (FBG) sensors to monitor impact damage and fatigue test of a composite wing structure. FBG sensors were able to monitor large scale composite structure for a long term, compared with non-destructive inspection (NDI) technologies such as acoustic emission (AE) sensors, an ultrasonic C-scan, and pulsed heating thermography. Ihn and Chang [33] applied their own damage index, ratio of the scatter energy contained in the  $S_0$  mode wave packet to the baseline energy contained in the  $S_0$  mode wave packet, for fatigue crack growth in a metallic structure. Their damage index showed the good correlation with the actual fatigue crack growth. Lissenden *et al.* [29] applied SDC for fatigue damage in composites and SDC was able to detect the damage at early stage. In this thesis, three point bending fatigue test was conducted on a composite beam with and without delamination damage, and SDC and NCM damage indexes were used to monitor the damage.

## 2.5 Finite element analysis

Finite element analysis has been performed over the past 40 years since simulations help us to understand the behavior of a structure in SHM. Kessler *et al.* [11] modeled a 2-D composite plate to obtain natural frequencies and mode shapes. EI-Kafrawy [34] also simulated natural frequencies and mode shapes of 3-D beams with a crack. Sorohan *et al.* [35] showed the

potential of a numerical simulation to get dispersion curves of Lamb wave. As mentioned in section 2.1, Lamb waves are dispersive in nature. Knowledge of dispersion curves is essential in an experiment to know which frequency has the best dispersion characteristics for a specific composite laminate in an experiment. Lissenden *et al.* [29] performed a numerical simulation to understand the effects of fatigue damage. They assumed fatigue damage was primarily composed of matrix crack and delamination and that it decreased the laminate stiffness and Poisson ratio. In their simulation, they degraded the modulus of the composites to monitor fatigue damage. In this thesis, a similar numerical simulation of fatigue damage for composite beams was conducted to comparatively evaluate the accuracy of NCM damage index.

## CHAPTER 3

### EXPERIMENTAL ANALYSIS

This chapter includes the fabrication of composite beams, data acquisition setup, experimental setup, and experimental results.

#### 3.1 Fabrication of composite specimens

There are several methods to fabricate composite materials: auto-clave molding, resin transfer molding (RTM), vacuum assisted resin transfer molding (VARTM), hand layup, and filament winding method. In this study, hand layup followed by compression during cure was used to produce laminates with good consolidation.

Carbon fibers fabric, IM7 (Hexcel Corporation), and resin, SC780 (Applied Poleramic Inc.), were used for fabricating composite plates with orientation  $[0_6/90_4/0_6]$  with no delamination, and 50.8 mm (2 inch) length delamination. Our fabrication process composed of cutting carbon fiber fabric, surface mold preparation, resin preparation, painting resin on a composite laminate, applying compression, and post curing. The carbon fiber fabric was cut into 304.8 mm  $\times$  304.8 mm (12 inch  $\times$  12 inch) squares. Teflon sheets of thickness 0.0127 mm (0.0005 inch) was inserted at the laminate mid-plane (between 8th layer and 9th layer) and to simulate delamination as shown in Figure 3.1.

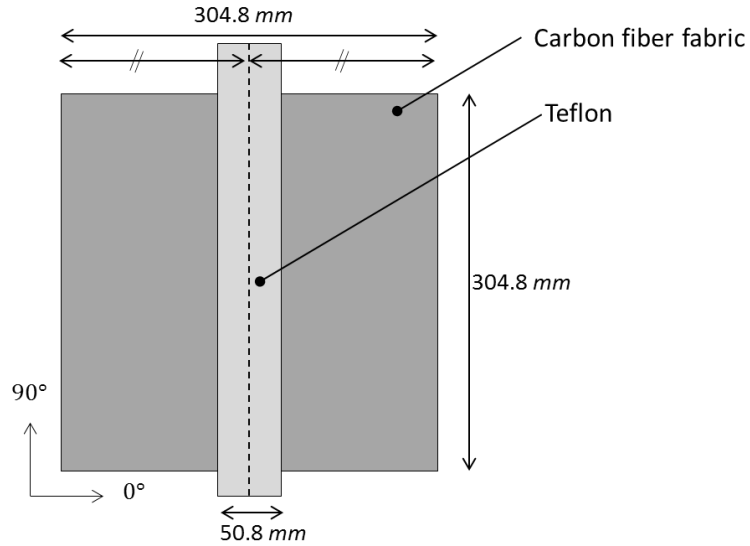


Figure 3.1 Schematic view of simulated delamination

Surface mold (Figure 3.2) was prepared by heating up to 150 °C in the oven because our spray release agent (Loctite Frekote 800 NC) works properly at that temperature.

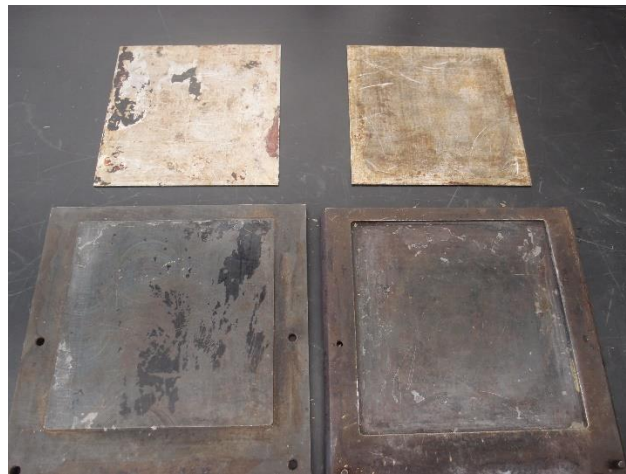


Figure 3.2 Surface mold

SC780 resin composed of two part epoxy-resin and-one part hardener was used as matrix material. Assuming the carbon fiber volume and the SC780 resin volume were 70% and 30 % out of the total volume of the composite plate, the weight of resin and hardener were calculated as follows. Firstly, the volume of carbon fibers was calculated:  $\text{Volume} = \text{Length} \times \text{Width} \times \text{Thickness}$ . Then, the volume of SC780 resin, three-sevenths of the volume of carbon fibers, was

calculated, and multiplying it by the density,  $1.09 \frac{g}{ml}$ , gave the weight of SC780 resin. From the weight ratio of resin and hardener: 4:1, the weight of resin and hardener used were 56.7 g and 12.5 g, respectively. All 16 layers of carbon fiber fabric were stacked on surface mold with SC780 resin brushed onto the fabric. The surface mold was put in the compression machine whose temperature and load were 38 °C and 5000 lbs to cure the SC780 resin for two hours under compression. The composite plate was then post cured in an oven heated at 73 °C for six hours. Finally, the composite plate was cut into 8 rectangular composite beams 228.6 mm (9 inch) in length by 25.4 mm (1 inch) in width for 3-point bending experiment. The eight replicate specimens of the undamaged baseline beam had no built-in delamination, while the eight replicate specimens of the “damaged” beam specimens had 50.8 mm length  $\times$  25.4 mm width (2 inch  $\times$  1 inch) delamination.



Figure 3.3 Composite specimens

### 3.2 Data acquisition setup

A NI PCI-6711 data acquisition (DAQ) card was used to generate a desired tone burst signal, an A-301 HS amplifier was used to amplify the tone burst signal up to  $\pm 175$  V before sending the signal to PZT actuators and a NI PXI-6250 DAQ card with 16-bit resolution and a high frequency sampling rate (up to 1.25 MHz) was used to measure the acquired voltage. In our study, the sampling rate used was 1 MHz, and National Instruments LabVIEW software was used to synchronize the initiation of the actuation and the DAQ card. The schematic view of data acquisition set up is shown in Figure 3.4.

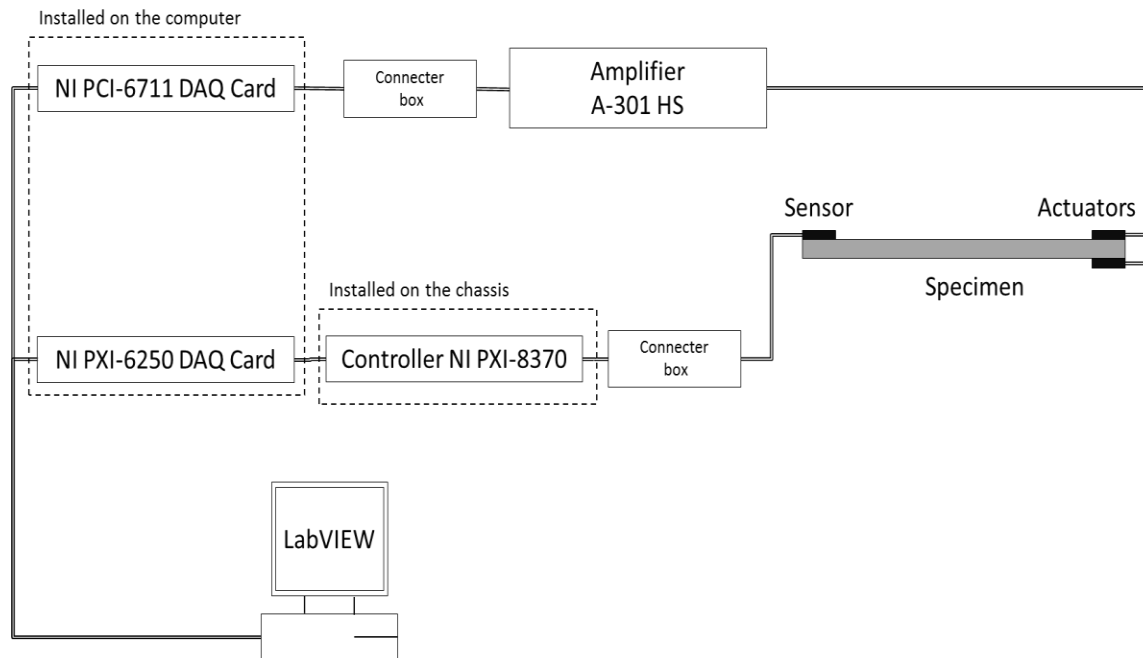


Figure 3.4 Schematic view of data acquisition set up

A PZT sensor mounted on the end of the composite beam was used to acquire the transmitted signal. A signal was applied to two PZT actuators mounted at the top and bottom surface of the other end of the composite beam as shown in Figure 3.5. PZT sensors (T216-A4NO-273X, Piezo Systems Inc.) used are 0.41 mm (0.016 inch) in thickness and 12.7 mm (0.5 inch) in diameter.

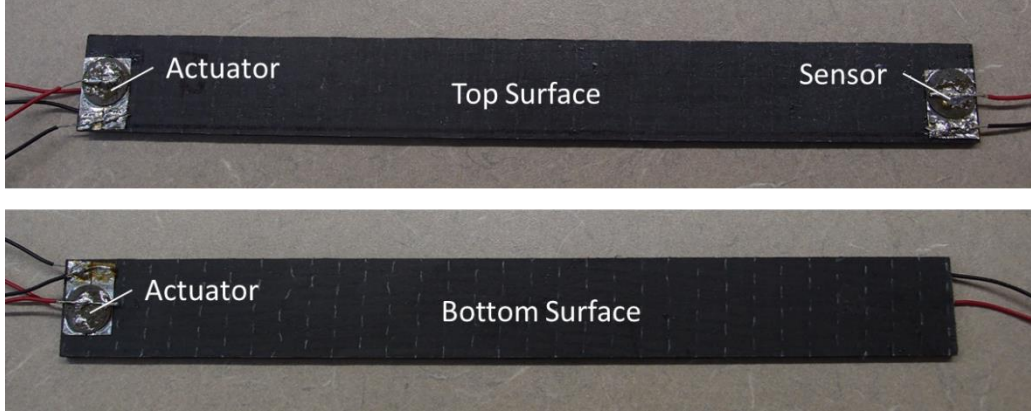


Figure 3.5 Test specimen with three PZTs

As an excitation signal, the tone burst was used and is defined by Equation (3.1).

$$f(t) = \begin{cases} wA\sin(\omega t) = wA\sin(2\pi f_c t), & 0 \leq t \leq t_1 \\ 0, & \text{otherwise} \end{cases} \quad (3.1)$$

where  $f(t)$  is the signal amplitude at time  $t$ ,  $w$  is the Hanning window function defined by Equation (3.2),  $A$  is the maximum amplitude,  $f_c$  is the center frequency of the tone burst, and  $t_1$  is the total signal time.

$$w(n) = 0.5 \times \left( 1 - \cos\left(\frac{2\pi n}{N-1}\right) \right), \quad 0 \leq n \leq N-1 \quad (3.2)$$

where  $N$  is the number of sampling points.

In this study, a tone burst having 5 cycles with a center frequency of 50 kHz and the maximum amplitude 1, was used as an excitation signal as shown in Figure 3.6. A high frequency Lamb wave (more than 200 kHz) is good for SHM to get high resolution results and avoid interference with flexural mode of the structure [36] but the center frequency used is 50 kHz because of the limitation of our data (DAQ) card. Anti-phase equal amplitude signals were applied to two actuators to generate an anti-symmetric ( $A_0$ ) Lamb wave mode. At low frequency, an anti-symmetric ( $A_0$ ) Lamb wave mode has shown the good sensitivity to small damage and delamination because it has lower phase velocity and wavelength than a symmetric ( $S_0$ ) mode [37] and propagates long distance with little dispersion [38].

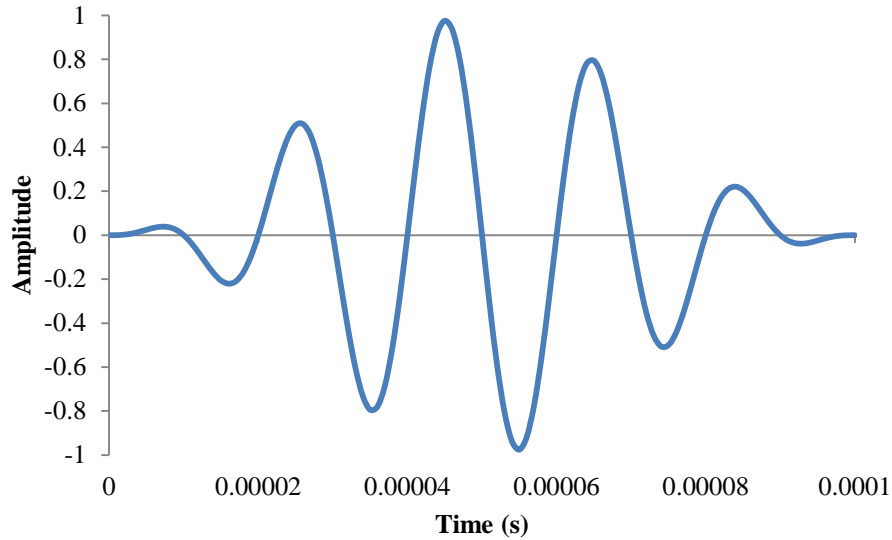


Figure 3.6 Tone burst having 5 cycles with a center frequency of 50 kHz

### 3.3.1 Experimental setup

Three point bending fatigue tests were performed to introduce fatigue defects in composite specimens. Fatigue load was measured by an MTS 661.18H-02 load cell and was applied by the piston, and the maximum load which was 70% of the ultimate strength, the stress ratio, and the loading frequency were 280 *N* (63 *lbs*), 0.1, and 1.0 Hz, respectively. LabVIEW code was written to acquire the load and displacement during fatigue tests and applied blocks of 500 cycles, and then SHM was performed at the mean load. Averaging technique written in LabVIEW code was used to reduce the signal noise. This process was repeated until the specimen was broken. Anti-phase excitation signals were applied to two PZT actuators mounted on the end of the composite beam. The schematic view of experimental setup is shown in Figure 3.7.

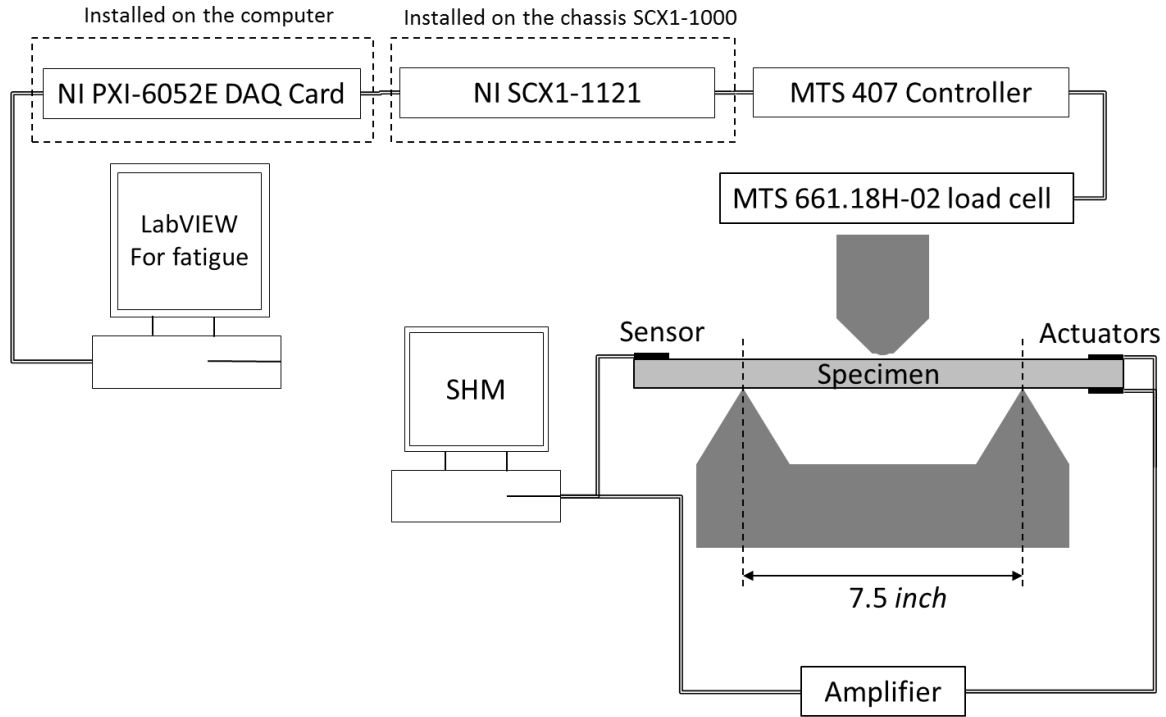


Figure 3.7 Schematic view of experimental setup

### 3.4 Experimental results

Fatigue tests were performed on three intact specimens to obtain a baseline for reference and on three specimens with  $50.8 \text{ mm}$  ( $2 \text{ inch}$ ) length delamination to evaluate the validity of NCM and SDC damage indices for the fatigue damage growth. Delamination growth was observed by taking pictures. Stiffness degradation was verified by the load at the valley divided by the deflection at the valley as shown in Figure 3.8. NCM and SDC calculated for three specimens are shown in Figure 3.9 and Figure 3.10, respectively and least squares curve are also plotted. Note that there were no differences between the orders of the statistical moment of NCM. Both NCM and SDC indices showed the highest value when specimens were broken. Though SDCs were almost constant before specimens failed, least squares curves of NCM for two different damaged specimens ('NCM-1-least squares curve' and 'NCM-3-least squares

curve' in Figure 3.9) were increasing. Thus, NCM showed better results than SDC for identifying fatigue damage growth.

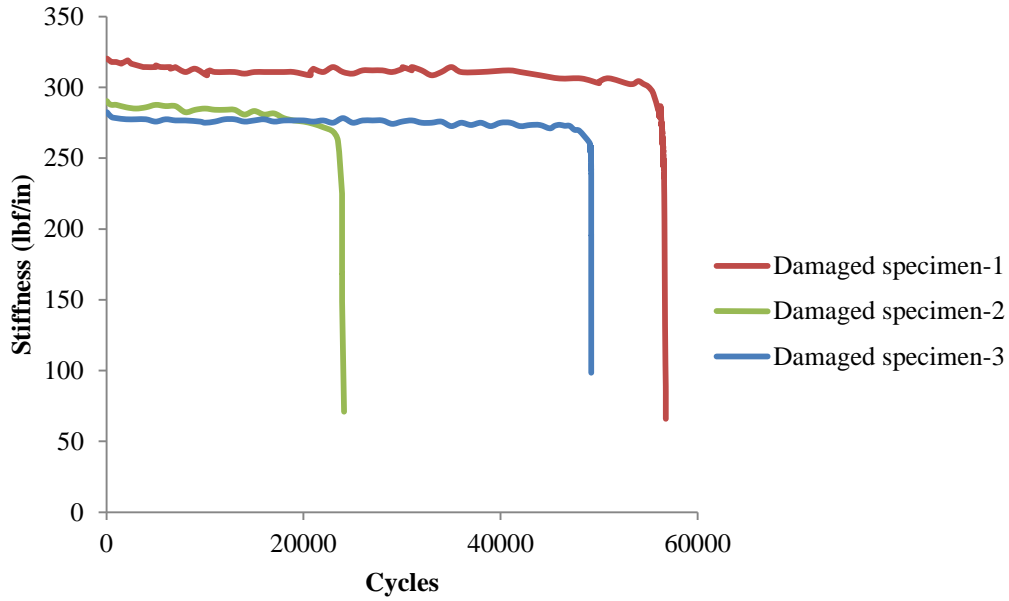


Figure 3.8 Stiffness degradation for three damaged specimens

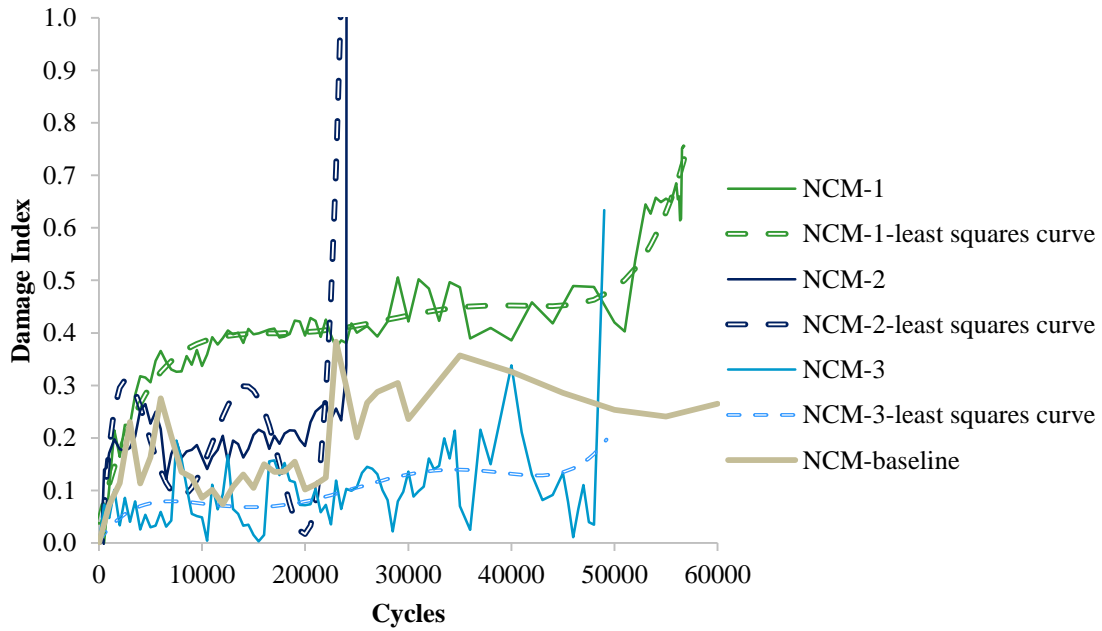


Figure 3.9 NCM for three damaged specimens

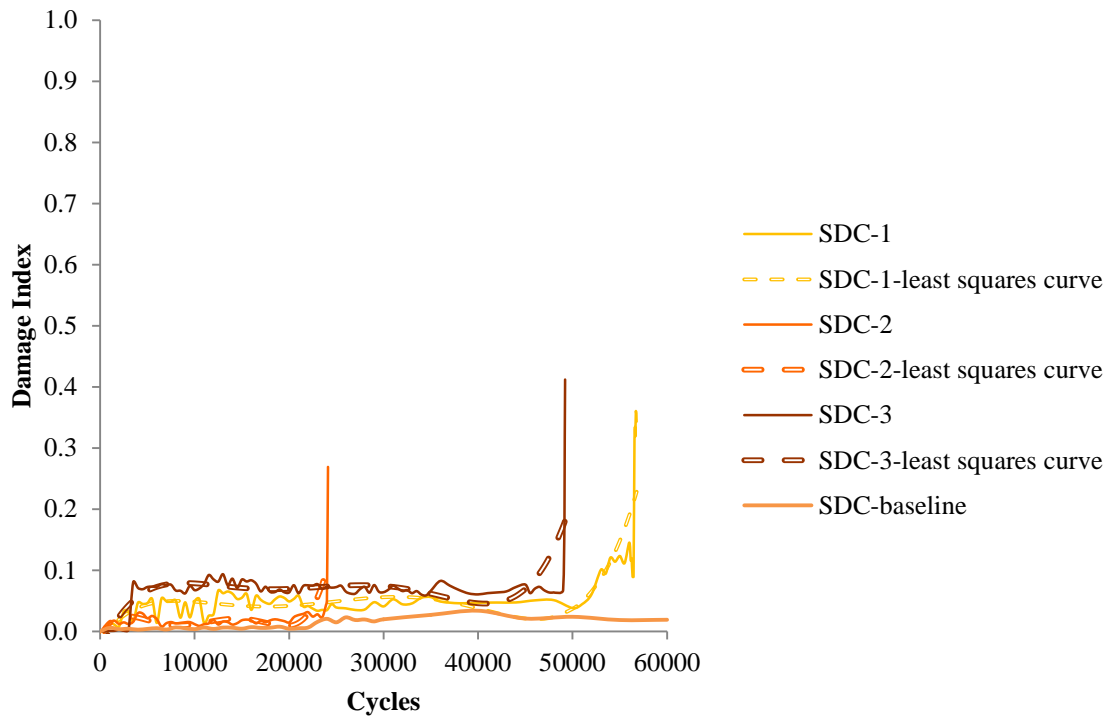


Figure 3.10 SDC for three damaged specimens

## CHAPTER 4

### SIMULATION ANALYSIS

This chapter provides simulation results including composite and delamination modeling benchmark test, Lamb wave propagation test, and fatigue damage detection using Lamb wave. A commercial finite element code, ABAQUS version 6.13, was used to conduct the simulation. Benchmark tests were performed to verify the modeling process.

#### 4.1 Composite and delamination modeling benchmark test

For the model verification and mesh convergence study, the structure chosen was a laminated composite cantilever beam subjected to a resultant shear load of 1 N at its end shown in. The thickness of each lamina was 0.3 mm and the stacking sequence was  $[0/90_2/0]$ . Its dimensions were  $50 \times 10 \times 1.2 \text{ mm}^3$  (Figure 4.2) made of Carbon/Epoxy IM7-8552 whose properties are shown in Table 4.1.

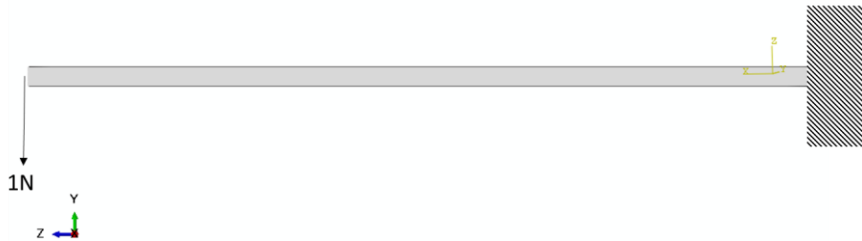


Figure 4.1 Composite cantilever beam subjected to a resultant shear load 1 N at its end

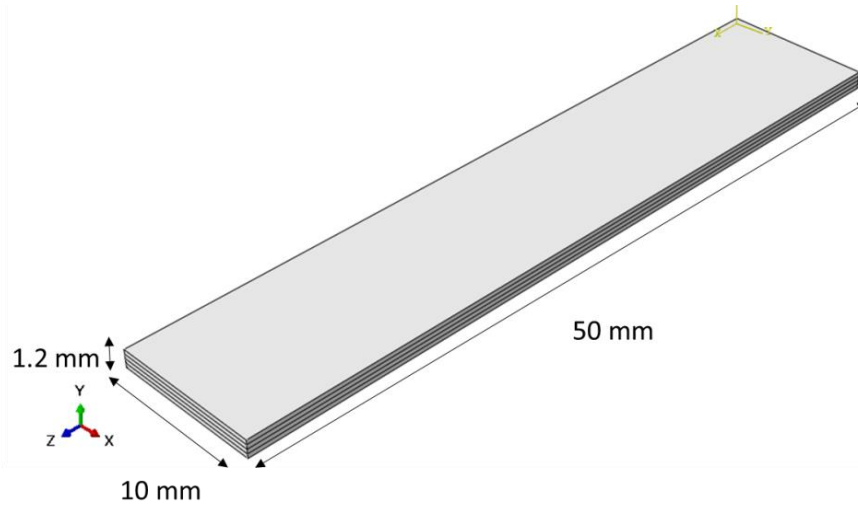


Figure 4.2 Dimensions of the composite cantilever beam with  $[0/90_2/0]$  orientations

Table 4.1 Material properties of IM7-8552

$E_1$ (GPa)	$E_2$ (GPa)	$E_3$ (GPa)	$\nu_{12}$	$\nu_{13}$	$\nu_{23}$	$G_{12}$ (GPa)	$G_{13}$ (GPa)	$G_{23}$ (GPa)
161.34	11.38	11.38	0.32	0.32	0.45	5.17	5.17	3.93

Various length of delamination: 2, 4, 6, 8, 10, 20 *mm* (width was always 10 *mm*), was introduced at the mid-plane of the beam (between 2th and 3th layer) at the mid-span. The model having 2mm length of delamination is presented in Figure 4.3.

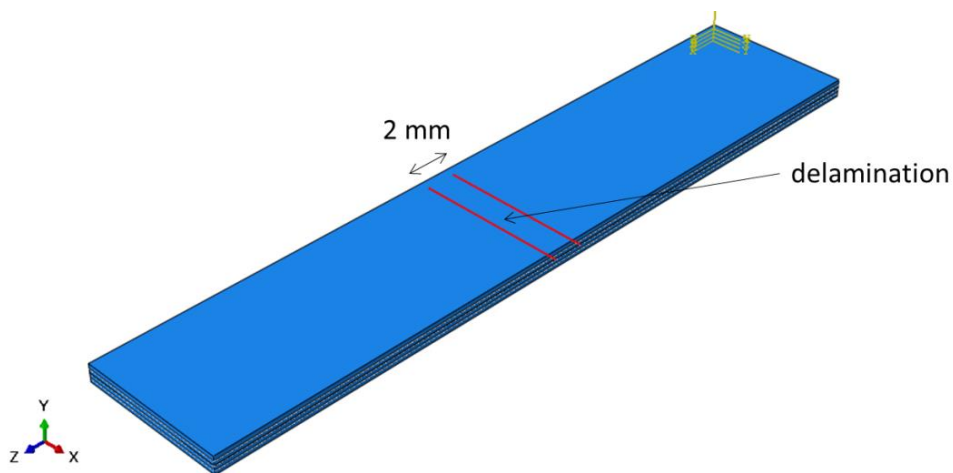


Figure 4.3 2mm length delamination at the mid span of the beam between 2th and 3th layer

Each layer was modeled by three-dimensional eight-node linear brick elements (C3D8). In the delamination area, the elements along the mid-plane were not tied and instead were assumed deboned by defining contact interaction in ABAQUS. The Euler-Bernoulli beam theory for a beam without delamination was used to compare the simulated results, and these results are shown in Table 4.2.

Table 4.2 Comparison of beam theory and simulation results

Delamination size (mm <sup>2</sup> )	Max deflection from FEA (mm)	Difference from Beam Theory (%)
No damage	0.19227	0.97
2×10	0.19234	1.01
4×10	0.19276	1.23
6×10	0.19384	1.79
8×10	0.19585	2.85
10×10	0.19910	4.56
20×10	0.24414	28.21
Beam theory (No delamination)	0.19042	

As expected, when the delamination size increases, deviation from beam theory prediction also increases. Comparing with the beam theory and the FEA model with no damage, the difference is a very low 0.97%, indicating good agreement with the simulation and theory. Thus, in all of the subsequent exercise, this composite modeling process and FEA mesh was used.

## 4.2 Lamb wave propagation test

Lamb wave propagation was simulated and SDC and NCM were calculated in this section using the validated FEA model. A  $228.6 \times 25.4 \times 3 \text{ mm}^3$  ( $9 \times 1 \times 0.1 \text{ inch}^3$ ) composite laminate made of IM7-8552 with  $[0_6/90_4/0_6]$  orientations was modeled using three dimensional eight-node linear brick elements (C3D8R) shown in Figure 4.4. Two models were created: One is the undamaged model and the other has a full width,  $25.4 \text{ mm}$  ( $1 \text{ inch}$ ) length delamination at the mid-plane of the beam (between 8th and 9th layer) at the mid-span, and the displacements in x, y, and z directions are constrained at the left surface of 8th layer and the displacements in y and z directions are constrained at the right surface of 8th layer in order to prevent the model from moving and rotating as shown in Figure 4.5. ABAQUS/Explicit analyses were performed with a very small time step,  $dt = 5 \times 10^{-8} \text{ sec}$  in order to satisfy the Courant-Friedrichs-Lewy (CFL) condition [39] and were performed with very fine mesh: the number of nodes and elements are 52580 and 256116, respectively. An actuator and a sensor were modeled as a node that mimics an actuator and a sensor location. Two actuator nodes and six sensor nodes were created in total on both surfaces, and Figure 4.6 shows the location of an actuator and three sensors on top surface. No.2 sensor node in Figure 4.6 was used for receiving the wave and other sensor nodes were used for seeing the wave propagation. The location of them on bottom surface is the same to that on top surface. A tone burst signal having 5 cycles with a center frequency 50 kHz was used as the excitation signal and this signal was applied to both actuator nodes on top and bottom surface as two vertical unidirectional displacements with the maximum amplitude  $0.01 \text{ mm}$  to excite the  $A_0$  mode. This method, exciting only symmetric or anti-symmetric modes, is called pure excitation as shown in Figure 4.7.

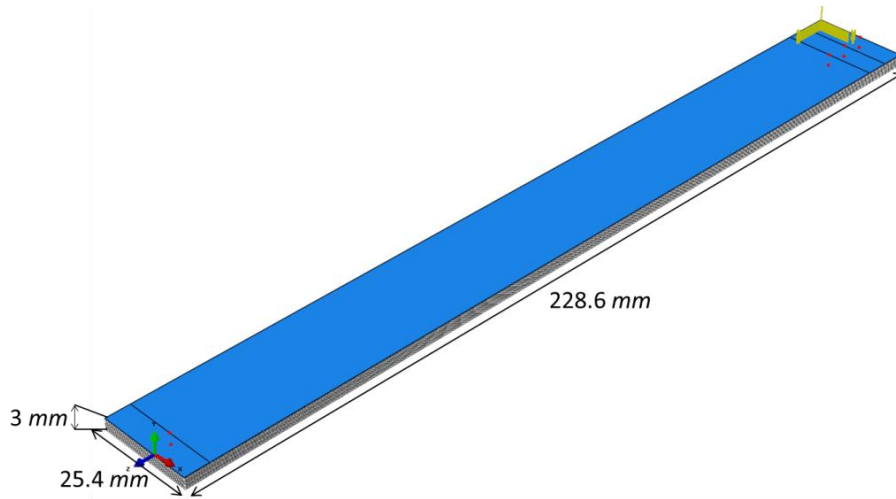


Figure 4.4 Dimensions of the composite laminate with  $[0_6/90_4/0_6]$  orientations

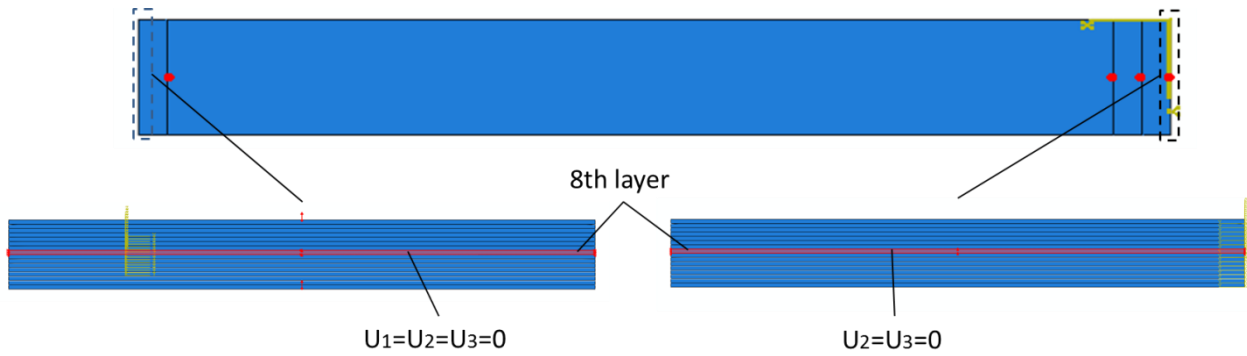


Figure 4.5 Boundary conditions of the composite laminate model



Figure 4.6 Location of actuators and three sensors on top surface

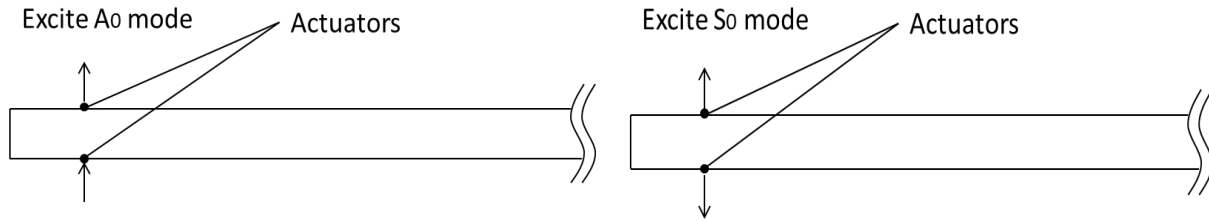


Figure 4.7 Pure excitation

The response from the No.2 sensor for both undamaged and damaged models is shown in Figure 4.8. SDC and NCM calculated are tabulated in Table 4.3. From the Table 4.3, both SDC and NCM can evaluate the delamination, and NCM (n=2) specially shows the highest value.

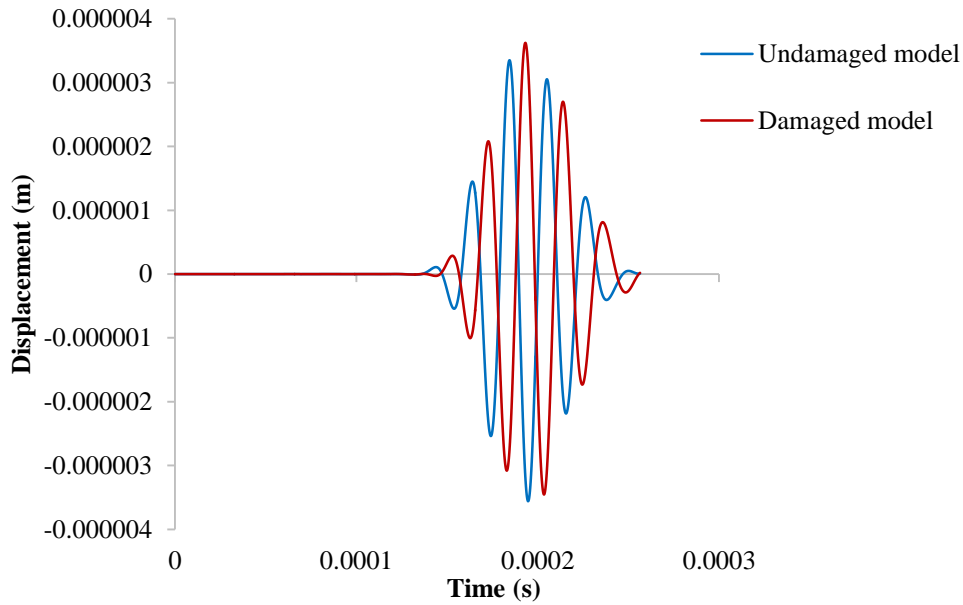


Figure 4.8 Response from the No.2 sensor for both undamaged and damaged model

Table 4.3 SDC and NCM for undamaged and damaged model

Damage Index	Comparison case
	Undamaged-damaged
SDC	0.1272
NCM (n=0.01)	0.0573
NCM (n=0.5)	0.1071
NCM (n=1)	0.1391
NCM (n=2)	0.1859

### 4.3 Fatigue damage detection using Lamb wave

Fatigue damage was simulated by reducing the material properties which has been commonly used in composite progressive failure analyses [40] [41] and by increasing the size of damage. Two models are considered: the model with reduced material properties is introduced in section 4.3.1 and the other with reduced material properties and increasing the size of damage is presented in section 4.3.2. All the models whose geometries, material properties, and an excitation signal are same as the one in section 4.2.

#### 4.3.1 Models with reduced material properties

Assuming fatigue damage reduces the stiffness of the matrix,  $E_m$ , the stiffness of the fiber,  $E_f$ , the stiffness of the matrix,  $E_m$ , and the Poisson's ratio of the matrix,  $\nu_m$ , tabulated in Table 4.4 were calculated using micromechanics. Note that the fiber's Poisson's ratio,  $\nu_f$ , and the fiber volume fraction,  $V_f$ , are assumed as 0.2 and 0.6, respectively.

Table 4.4 Material properties of IM7-8552 using micromechanics

$E_f$ (GPa)	$E_m$ (GPa)	$\nu_f$	$N_m$
266	4.7	0.2	0.5

The stiffness of the matrix,  $E_m$ , was degraded from 100% to 70% in 10% increments to simulate fatigue damage and then the longitudinal Young's modulus:  $E_1$  and the transverse Young's modulus:  $E_2$  were calculated and these values are used in ABAQUS. In the case of 70% of  $E_m$ ,  $E_1$  is 160.78 GPa and  $E_2$  is 8.03 GPa, for example. Two cases were studied: undamaged model and damaged model with 25.4 mm (1 inch) length delamination at the mid-plane of the beam (between 8th and 9th layer) at the mid-span. The responses from the No.2 sensor for four cases: The undamaged model, with 90% properties of the initial values, with 80% properties of the initial values, and with 70% properties of the initial values are presented in Figure 4.9. As the

material properties are degraded, the received waves are slightly shifted and are attenuated, and SDC and NCM increase. Those are plotted in Figure 4.10 and tabulated in Table 4.5.

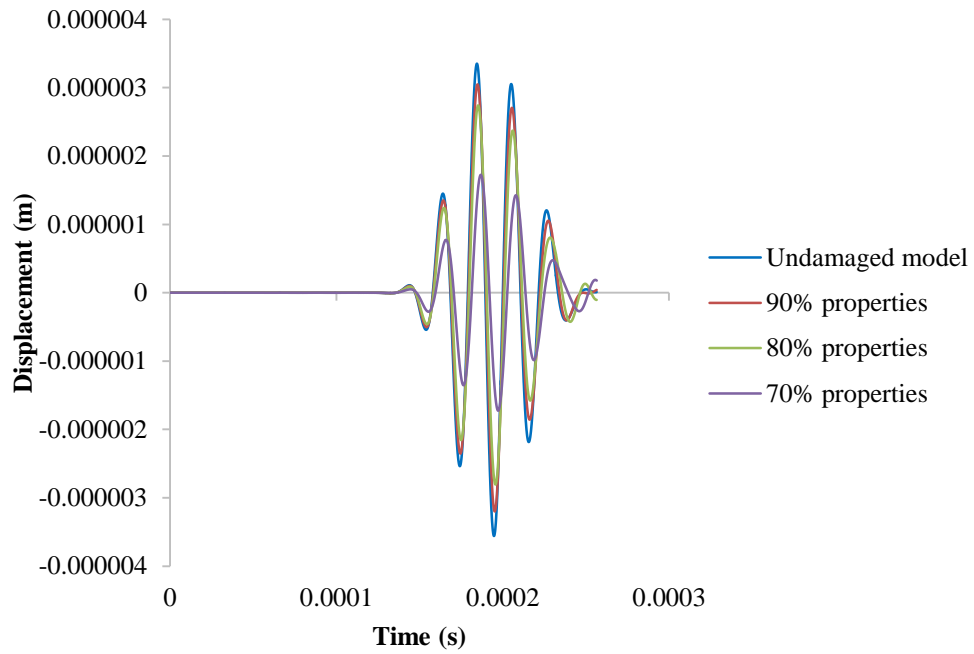


Figure 4.9 Response from the No.2 snesor for the undamaged model, with 90% properties, with 80% properties, and with 70% properties.

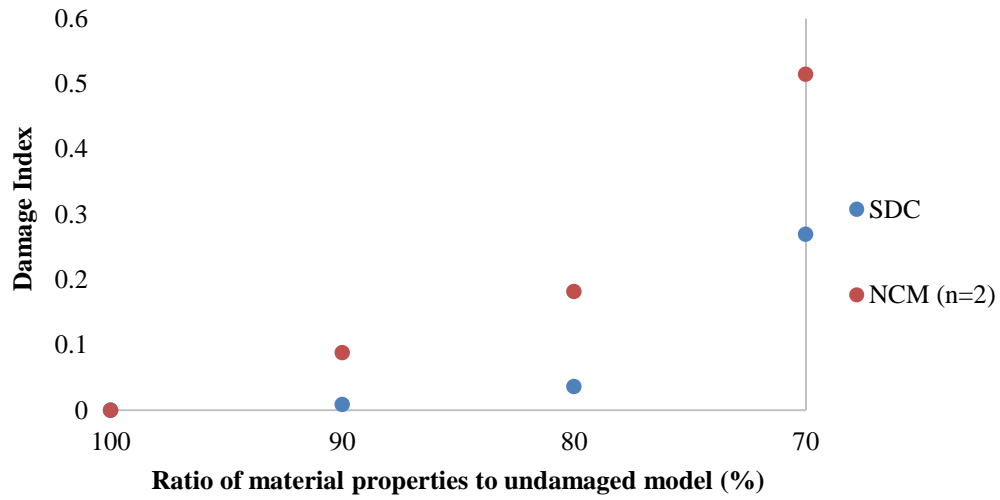


Figure 4.10 SDC and NCM (n=2) for three comparison cases: Undamaged-90% properties, Undamaged-80% properties, and Undamaged-70% properties

Table 4.5 SDC and NCM for three comparison cases: Undamaged-90% properties, Undamaged-80% properties, and Undamaged-70% properties

Damage Index	Comparison case		
	Undamaged-90% properties	Undamaged-80% properties	Undamaged-70% properties
SDC	0.00088	0.036	0.2693
NCM (n=0.01)	0.0986	0.2001	0.5244
NCM (n=0.5)	0.0918	0.1878	0.5118
NCM (n=1)	0.0897	0.1843	0.5124
NCM (n=2)	0.0882	0.1817	0.5146

As well as the undamaged model, the damaged model was also studied. The responses from the No.2 sensor for four cases: The damaged models, with 90% properties of the initial values, with 80% properties of the initial values, and with 70% properties of the initial values are shown in Figure 4.11. SDC and NCM are plotted in Figure 4.12 and tabulated in Table 4.6.

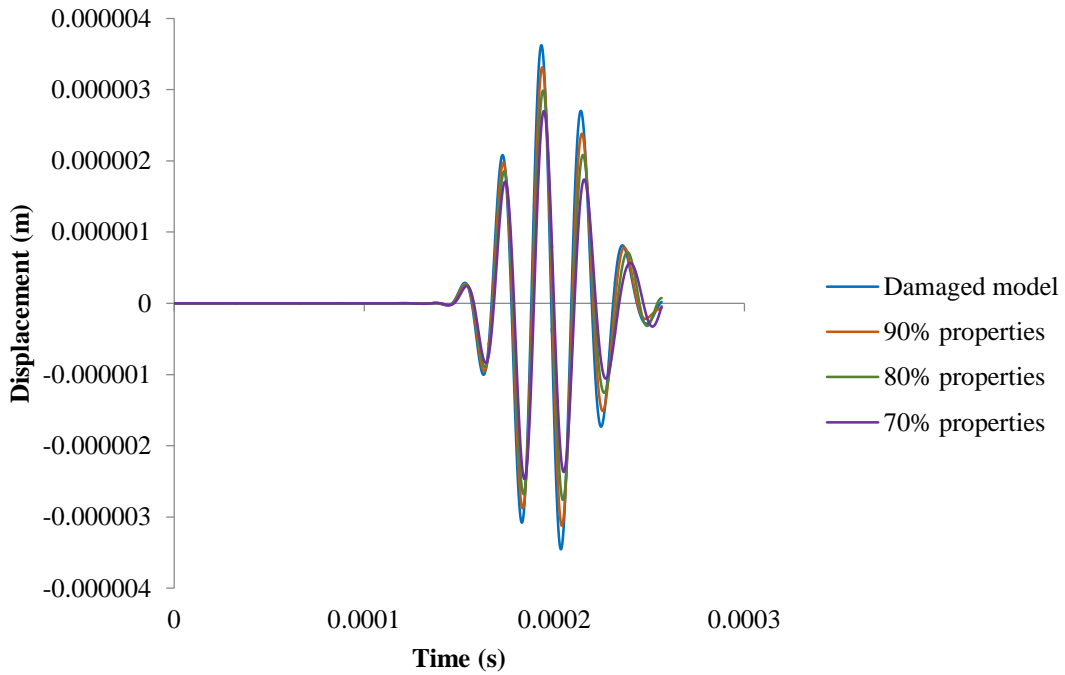


Figure 4.11 Response from the No.2 sensor for the damaged model, with 90% properties, with 80% properties, and with 70% properties.

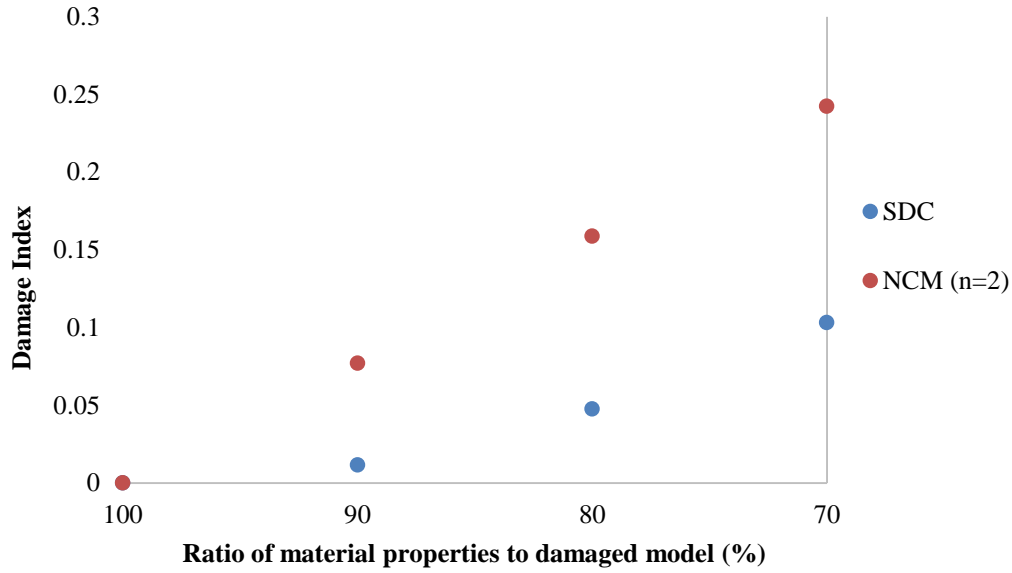


Figure 4.12 SDC and NCM (n=2) for three comparison cases: Damaged-90% properties, Undamaged-80% properties, and Undamaged-70% properties

Table 4.6 SDC and NCM for three comparison cases: Damaged-90% properties, Damaged-80% properties, and Damaged-70% properties

Damage Index	Comparison Case		
	Damaged-90% properties	Damaged-80% properties	Damaged-70% properties
SDC	0.0116	0.0477	0.1033
NCM (n=0.01)	0.0864	0.1758	0.2651
NCM (n=0.5)	0.0791	0.1622	0.2470
NCM (n=1)	0.0774	0.1594	0.2433
NCM (n=2)	0.0770	0.1588	0.2424

### 4.3.2 Models with reduced material properties and increasing size of damage

Assuming fatigue damage reduces the material properties and increases the size of damage, the material properties of all the models were set as 90% of the initial value and the size of damage was increased from 0.254 mm (0.01 inch) to 10.16 mm (0.4 inch) as shown in Figure 4.13. Here,  $\Delta a$  shows the increment of damage length size and damage is at the mid-span of the beam between 8th and 9th layer.

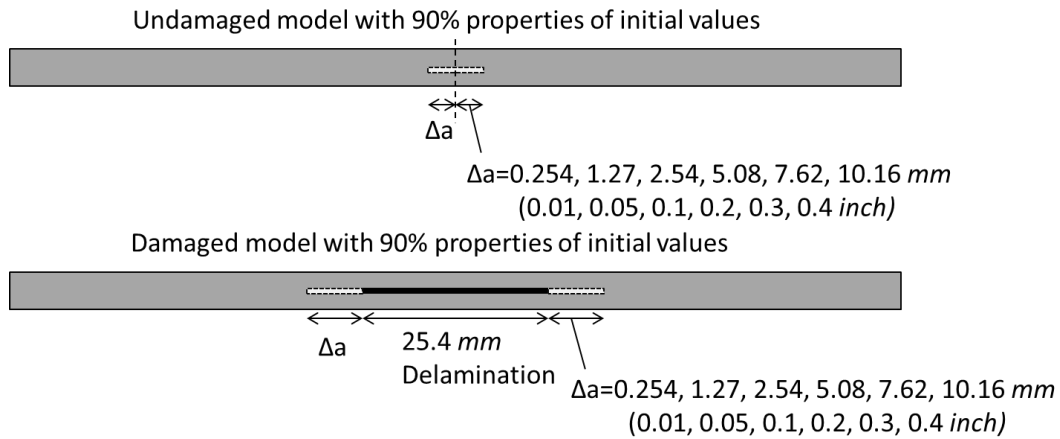


Figure 4.13 Schematic view of undamaged and damaged models with reduced material properties and increasing size of damage

The responses from No.2 sensor for seven cases: the undamaged model, with 0.254 mm damage, with 1.27 mm damage, with 2.54 mm damage, with 5.08 mm damage, with 7.62 mm damage, with 10.16 mm damage are shown in Figure 4.14 and SDC and NCM are plotted in Figure 4.15 and tabulated in Table 4.7, respectively. As damage size increases, the signal is shifted and that amplitude increases.

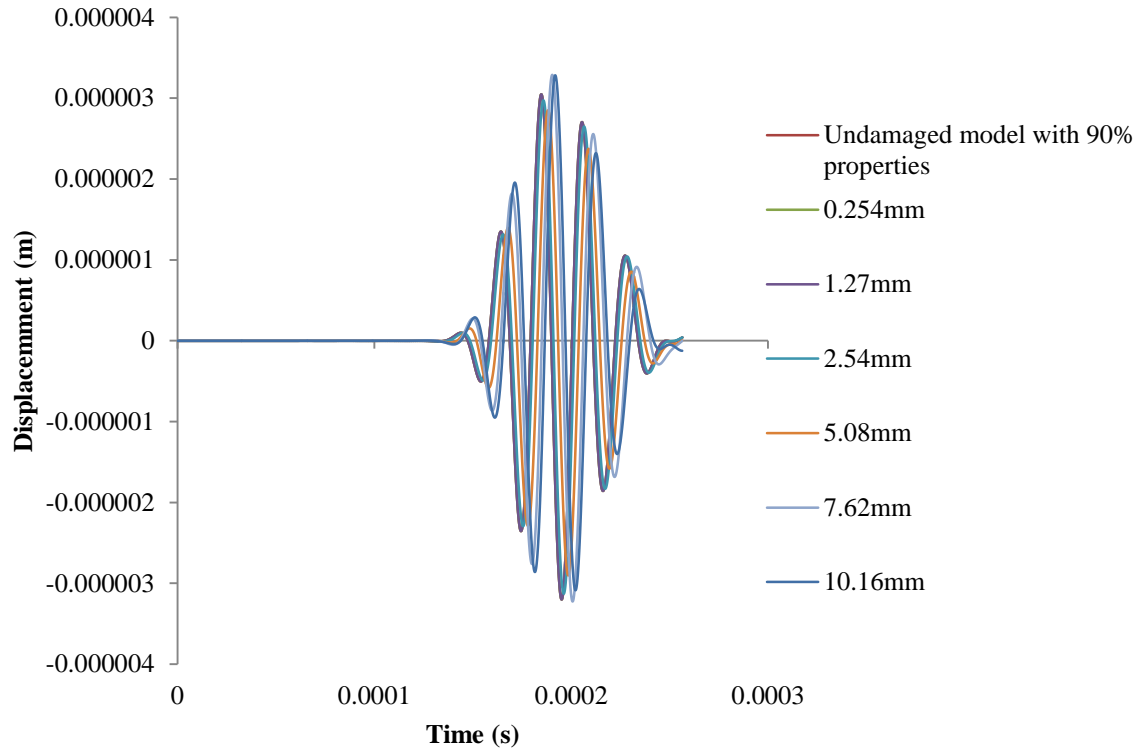


Figure 4.14 Responses from No.2 sensor for undamaged model with 90% material properties, with 0.254 mm damage, with 1.27 mm damage, with 2.54 mm damage, with 5.08 mm damage, with 7.62 mm damage, and with 10.16 mm damage

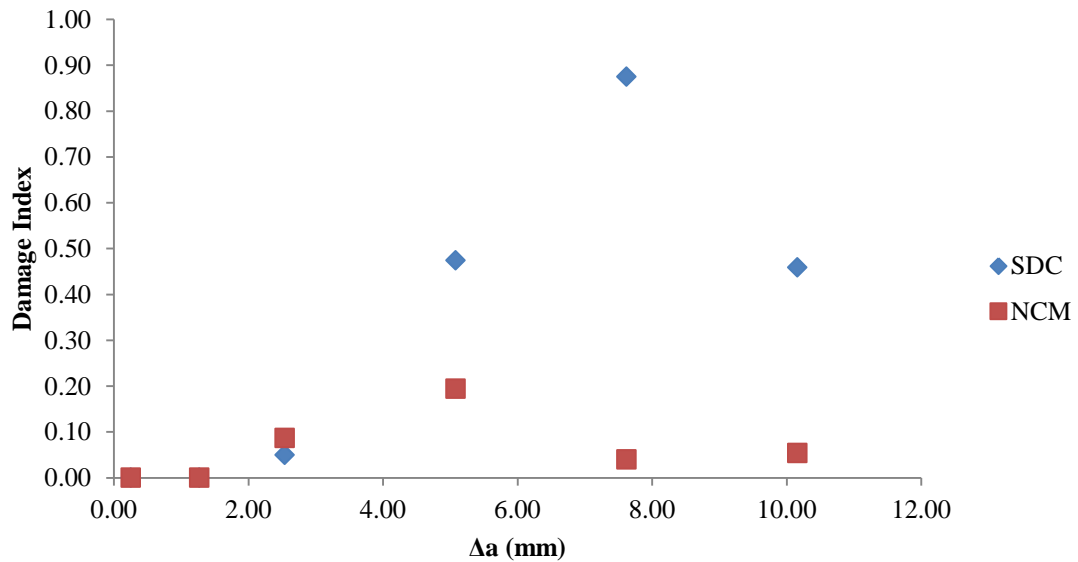


Figure 4.15 SDC and NCM (n=2) for six cases: Undamaged-0.254 mm, Undamaged-0.127 mm, Undamaged-5.08 mm, Undamaged-7.62 mm, and Undamaged-10.16 mm

Table 4.7 SDC and NCM for six cases: Undamaged-0.254 mm, Undamaged-0.127 mm, Undamaged-5.08 mm, Undamaged-7.62 mm, and Undamaged-10.16 mm

Damage Index	Comparison case					
	Undamaged-0.254mm	Undamaged-1.27mm	Undamaged-2.54mm	Undamaged-5.08mm	Undamaged-7.62mm	Undamaged-10.16mm
SDC	5.18E-07	5.18E-07	0.0499	0.4740	0.8751	0.4590
NCM (n=0.01)	1.03E-04	1.03E-04	0.0687	0.1640	0.0112	0.0116
NCM (n=0.5)	1.13E-04	1.13E-04	0.0652	0.1516	0.0004	0.0181
NCM (n=1)	1.29E-04	1.29E-04	0.0717	0.1668	0.0209	0.0373
NCM (n=2)	1.60E-04	1.60E-04	0.0868	0.1940	0.0400	0.0540

As well as the above, the responses from No.2 sensor for damaged model are shown in Figure 4.16 and SDC and NCM are plotted in Figure 4.17 and tabulated in Table 4.8, respectively. As damage size increases, the signal is shifted and that amplitude increases.

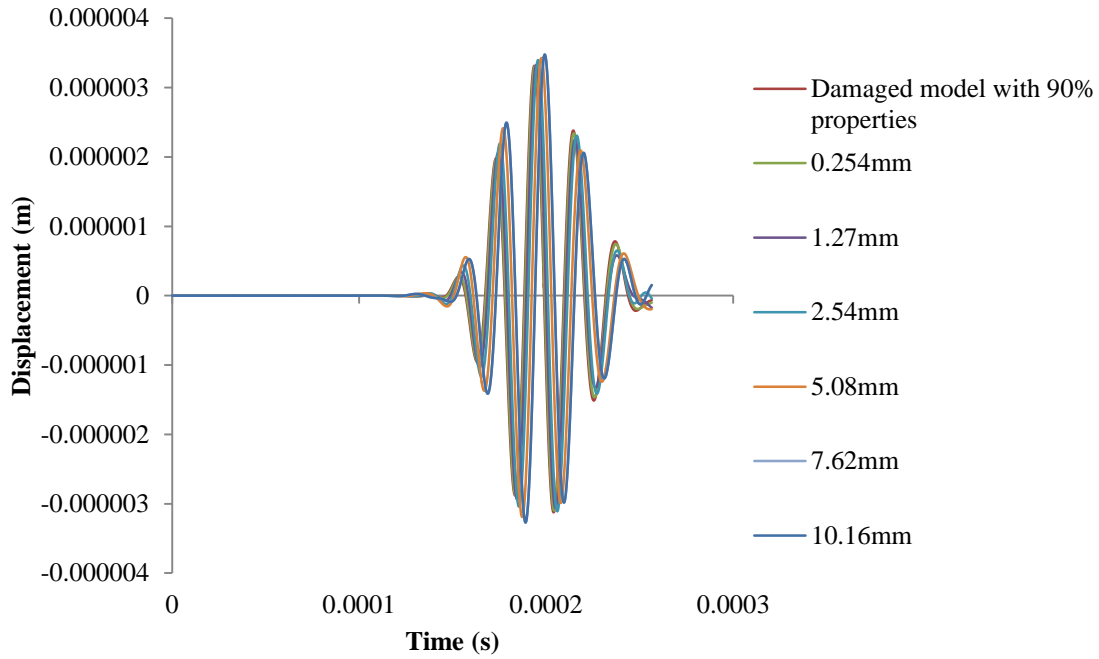


Figure 4.16 Responses from No.2 sensors for damaged model with 90% material properties, with 0.254 mm damage, with 1.27 mm damage, with 2.54 mm damage, with 5.08 mm damage, with 7.62 mm damage, and with 10.16 mm damage

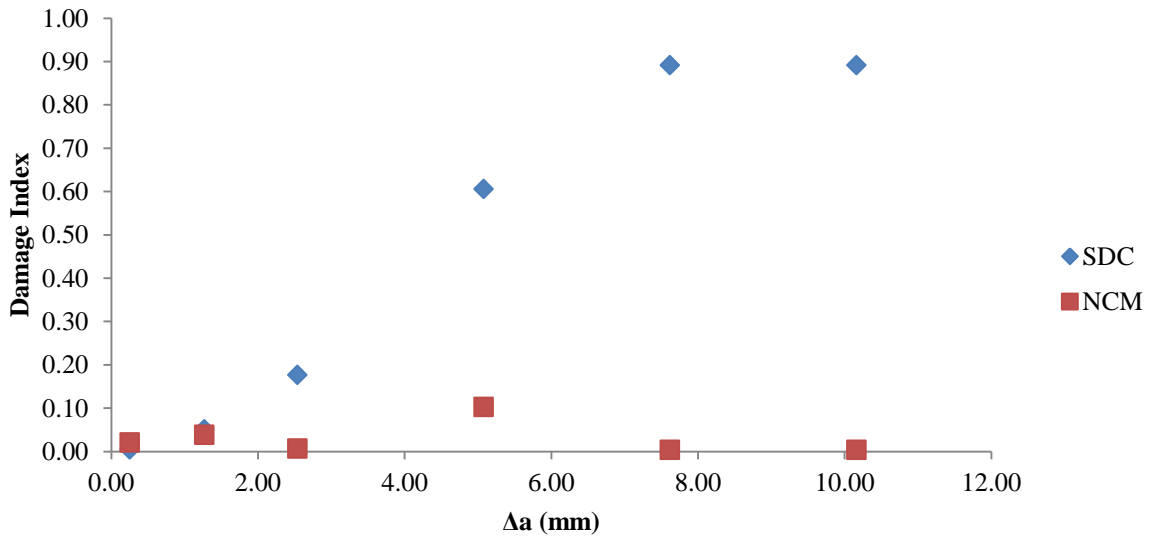


Figure 4.17 SDC and NCM (n=2) for six cases: Damaged-0.254 mm, Damaged-0.127 mm, Damaged-5.08 mm, Damaged-7.62 mm, and Damaged-10.16 mm

Table 4.8 SDC and NCM for six cases: Damaged-0.254 *mm*, Damaged-0.127 *mm*, Damaged-5.08 *mm*, Damaged-7.62 *mm*, and Damaged-10.16 *mm*

Damage Index	Comparison case					
	Damaged -0.254mm	Damaged -1.27mm	Damaged -2.54mm	Damaged -5.08mm	Damaged -7.62mm	Damaged -10.16mm
SDC	0.0046	0.0512	0.1770	0.6056	0.8914	0.8914
NCM (n=0.01)	0.0159	0.0349	0.0174	0.0238	0.0159	0.0159
NCM (n=0.5)	0.0141	0.0254	0.0060	0.0661	0.0120	0.0120
NCM (n=1)	0.0157	0.0281	0.0072	0.0754	0.0015	0.0015
NCM (n=2)	0.0207	0.0384	0.0067	0.1031	0.0039	0.0039

From Figure 4.15 and Figure 4.17, NCM does not show the higher values than SDC and shows the oscillating results. The reason of this will be discussed in the next chapter. SDC linearly increases at first but suddenly decreases at  $\Delta a = 10.16 \text{ mm}$  because it oscillates with respect to time of flight as mentioned in Figure 2.7. From this simulation, it is found that both NCM and SDC do not linearly increase with damage growth.

## CHAPTER 5

### RESULTS AND DISCUSSION

#### 5.1 Comparison of experimental and simulation results

FEM model was developed to compare experimental results with simulation results. The composite modeling process and FEA mesh were the same as in CHAPTER 4. A  $228.6 \times 25.4 \times 3 \text{ mm}^3$  ( $9 \times 1 \times 0.1 \text{ inch}^3$ ) composite laminate made of IM7-SC780 (Table 5.1) with  $[0_6/90_4/0_6]$  orientations was modeled using three dimensional eight-node linear brick elements (C3D8R).

Table 5.1 Material properties of IM7-SC780

$E_1$ (GPa)	$E_2$ (GPa)	$E_3$ (GPa)	$\nu_{12}$	$\nu_{13}$	$\nu_{23}$	$G_{12}$ (GPa)	$G_{13}$ (GPa)	$G_{23}$ (GPa)
113.633	5.239	5.239	0.354	0.354	0.55	3.1781	3.1781	1.6672

This finite element model has a prefabricated  $50.8 \text{ mm}$  ( $2 \text{ inch}$ ) length delamination at the mid-plane of the beam (between 8th and 9th layer) at the mid-span spanning across the width of the laminate as shown in Figure 5.1. The displacements in x, y, and z directions are constrained at the  $19.05 \text{ mm}$  ( $0.75 \text{ inch}$ ) place from the left on the bottom surface and the displacements in y and z directions are constrained at the  $19.05 \text{ mm}$  ( $0.75 \text{ inch}$ ) location from the right on the bottom surface to simulate the experimental boundary condition: bottom fixture supports the specimen. The displacement in y direction of the loading point at the center of the top surface was assigned the zero displacement constrained to simulate the boundary condition of the top fixture in the experiment. These boundary conditions are shown in Figure 5.2.

ABAQUS/Explicit analyses were performed with a very fine mesh: the number of nodes and elements are 52580 and 256116, respectively. The location of actuators and sensors in the FE model are identical to that in the Figure 4.6 in CHAPTER 4 and are indicated in Figure 5.2. A Hanning tone burst signal having 5 cycles with a center frequency of 50 kHz was used as the excitation signal and this signal was applied to both actuator nodes on top and bottom surface as two vertical displacements with the maximum amplitude 0.01 mm to excite the  $A_0$  mode.

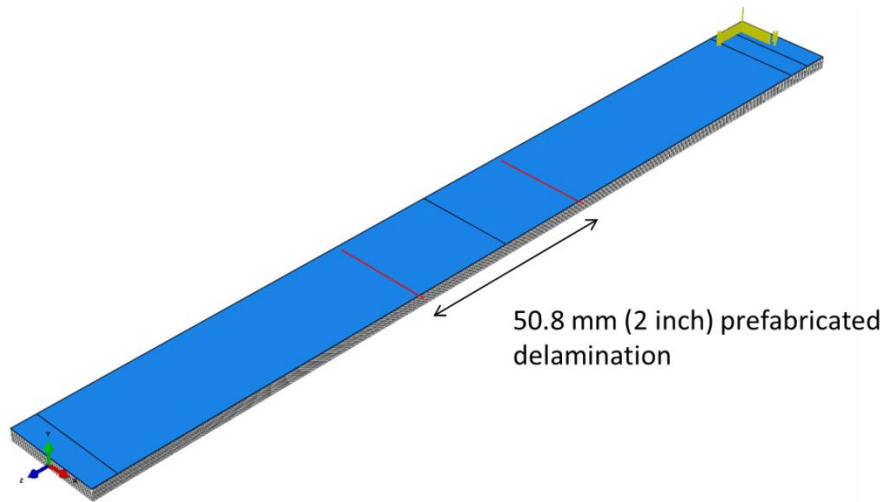


Figure 5.1 Prefabrocated 50.8 mm (2 inch) length delamination

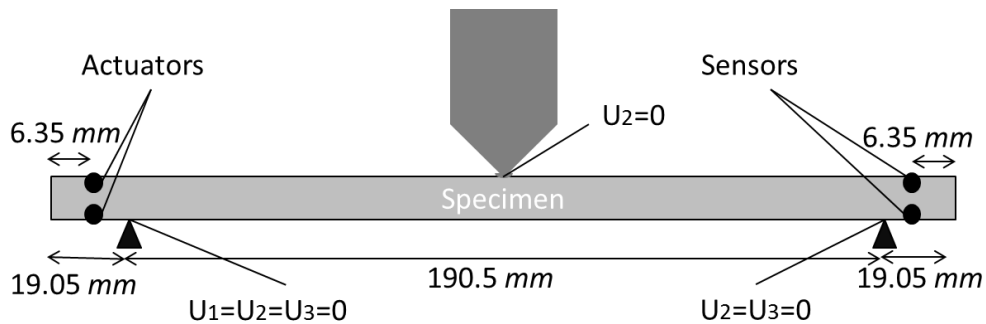


Figure 5.2 Side view of specimen showing boundary conditions of the FEA model for comparison with experimental results

Fatigue damage growth was simulated by increasing the size of delamination using the experimental results for delamination length as a function of the number of fatigue cycles.

Delamination growth vs. fatigue cycle for three specimens (same to the specimens used in the experiment) observed by taking pictures during the experiment is plotted and tabulated in Figure 5.3 and Table 5.2, respectively. The picture of the delamination growth for damaged specimen-2 is also shown in Figure 5.4.

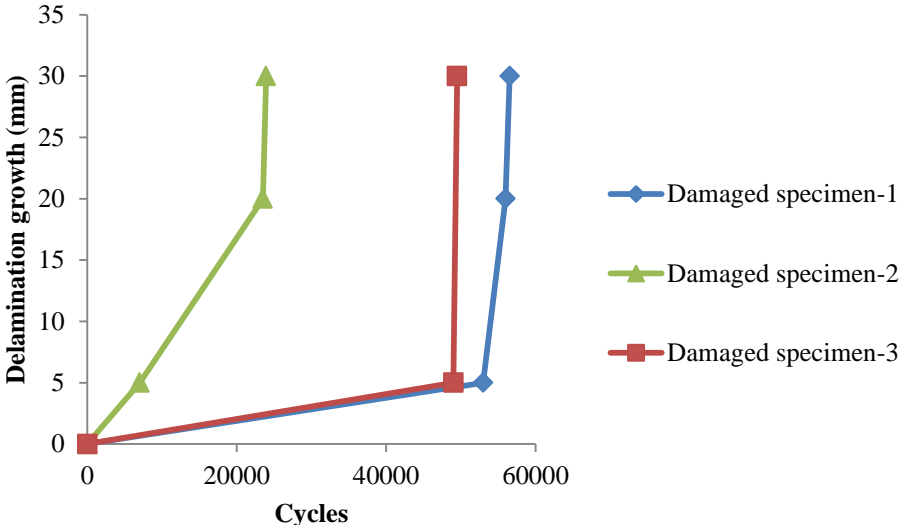


Figure 5.3 Delamination growth for three specimens observed in the experiment

Table 5.2 Delamination growth for three specimens observed in the experiment

Delamination growth(mm)	Damaged specimen-1	Damaged specimen-2	Damaged specimen-3
	Cycles		
0	0	0	0
5	53000	7000	49000
20	56000	23500	
30	56550	23916	49500



Figure 5.4 Delamination growth at 23500 cycles for damaged specimen-2

According to Figure 5.4, delamination growth was not symmetric about the load point during the experiment. In the FE model, this unsymmetrical delamination growth was simulated by extending deboned area as shown in Figure 5.5 using the UNTIE nodes command in ABAQUS. Contact elements were used to avoid penetration of the delaminated surfaces. Based on test data, it was assumed that the initial stiffness of the FE model was reduced by 10% due to the pre-existing 50.4 mm (2 inch) delamination before delamination growth occurred. Signal difference coefficient (SDC) and normalized correlation moment (NCM) were calculated for two specimens (Damaged specimen-2 and Damaged specimen-3) and compared with the experimental results as shown in Figure 5.6 and Figure 5.7, respectively. Here, specimens used in Figure 5.6 and in Figure 5.7 are corresponding with the specimens in Figure 3.9 and Figure 3.10. As can be observed, SDC data obtained from the FE model (symbols) shows very good correlation with the experimental results (line) for both composite damage specimens while NCM data obtained from the FE model (symbols) show a close trend to the experimental results (line) but the experimental data has more oscillations than that of the FE model. This will be discussed in the next section.

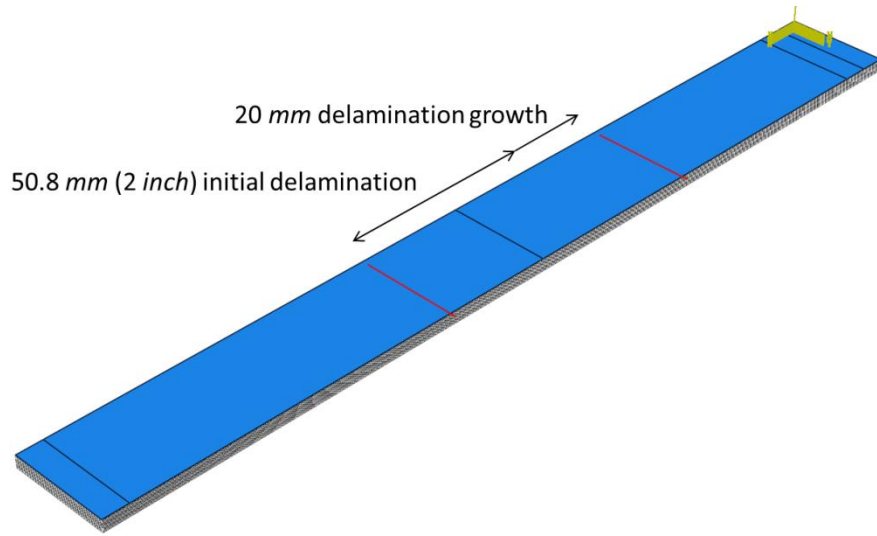


Figure 5.5 Simulating delamination growth in the FEA model

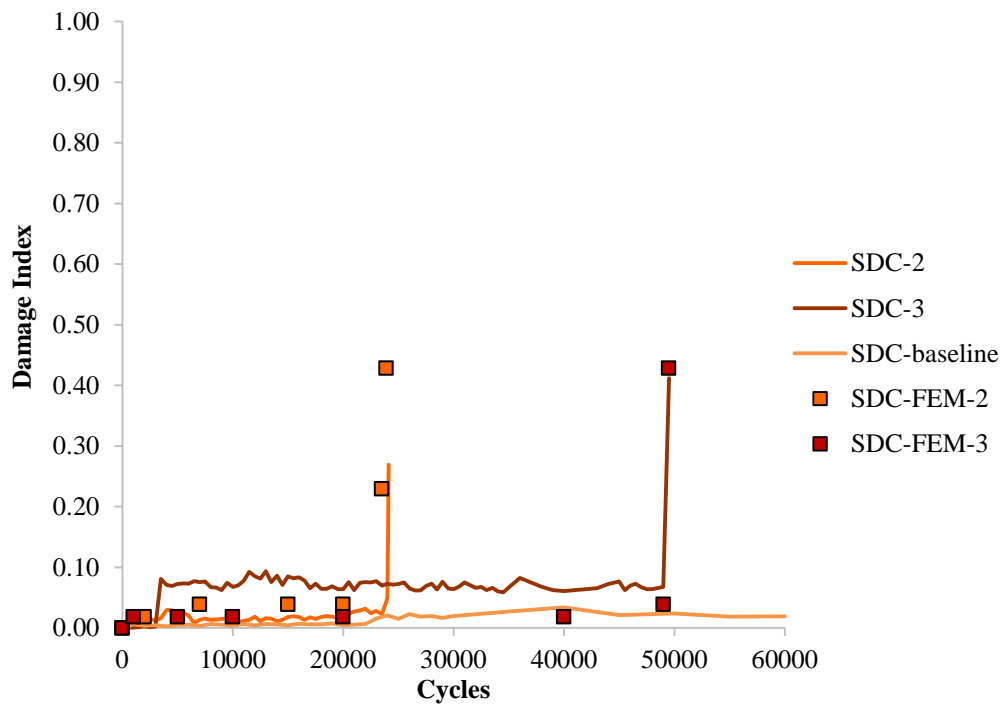


Figure 5.6 SDC for comparison of the experiment and the simulation

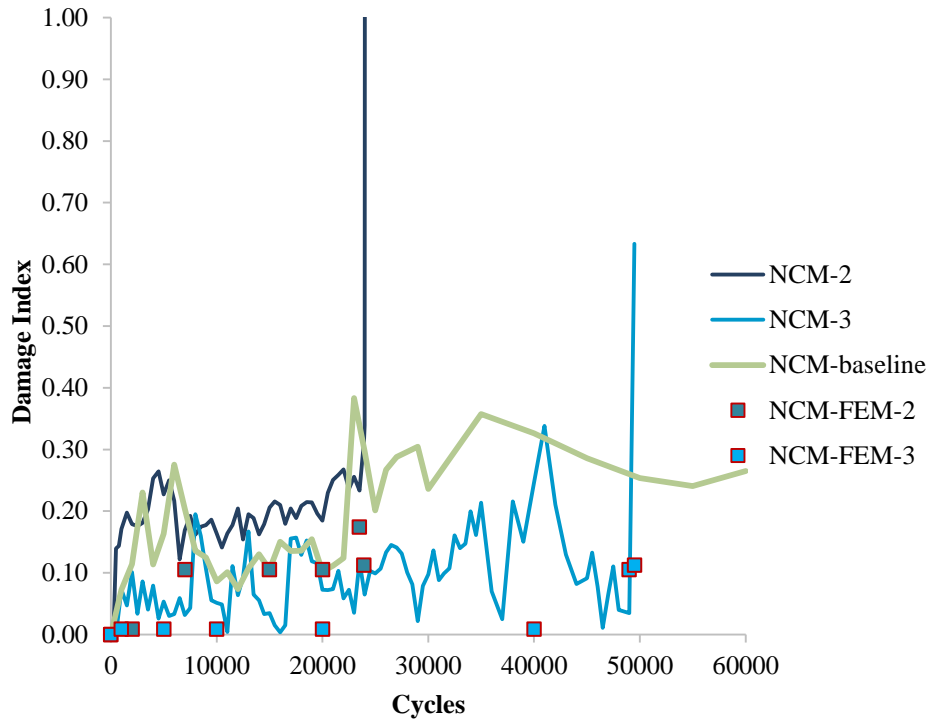


Figure 5.7 NCM for comparison of the experiment and the simulation

## 5.2 Validity of the NCM damage index for fatigue damage

According to Torkamani *et al.* [14], Normalized correlation moment (NCM) showed significant advantage for the identification of the delamination in composites under static loading because of its sensitivity to wave attenuation. However, in the present study, NCM displayed oscillating results for fatigue damage identification as shown in Figure 5.7. In order to confirm the validity of NCM for fatigue damage, sensitivity of NCM to time of flight and wave attenuation and wave amplitude increase was theoretically studied. Time of flight in the baseline signal is considered to be equal to the signal ( $T_{F_x} = T$ ) and the amplitude of the signal is 1, and that of the comparison signal is increased from  $T_{F_y} = T$  to  $T_{F_y} = 2T$  but the amplitude of the comparison signal is 0.7 (unlike as shown in Figure 2.7). As can be seen in Figure 5.8, NCM starts from 0.3 and monotonically increases. This means NCM properly monitors damage when time of flight and wave attenuation simultaneously occur. Similarly, sensitivity of NCM to time of flight and wave amplitude increase is shown in Figure 5.9. The amplitude of the comparison signal is 1.3. NCM starts from 0.3 and it decreases before increasing later, which means NCM cannot properly monitor damage when time of flight and wave increase simultaneously occur. This is the reason why NCM oscillated in the simulation in CHAPTER 4 because the amplitude of signals increased and signals were shifted as damage size increased.

During the experiment, the amplitude of the received signals was changed (Figure 5.10) though there was no damage growth because the specimen was slightly bent by the applied force during SHM. This amplitude changes during SHM caused different values of NCM every time though there were no damage growth, which made NCM oscillate.

From these results, when time of flight and wave increase occur at the same time, it gives rise to oscillations in NCM damage index and nonplanar of a specimen affects NCM

results. These oscillations in NCM are observed both the experiments and the simulations. On the other hand, because SDC is not very sensitive to wave attenuation and increase but sensitive to the time of flight, SDC shows more stable results for fatigue damage.

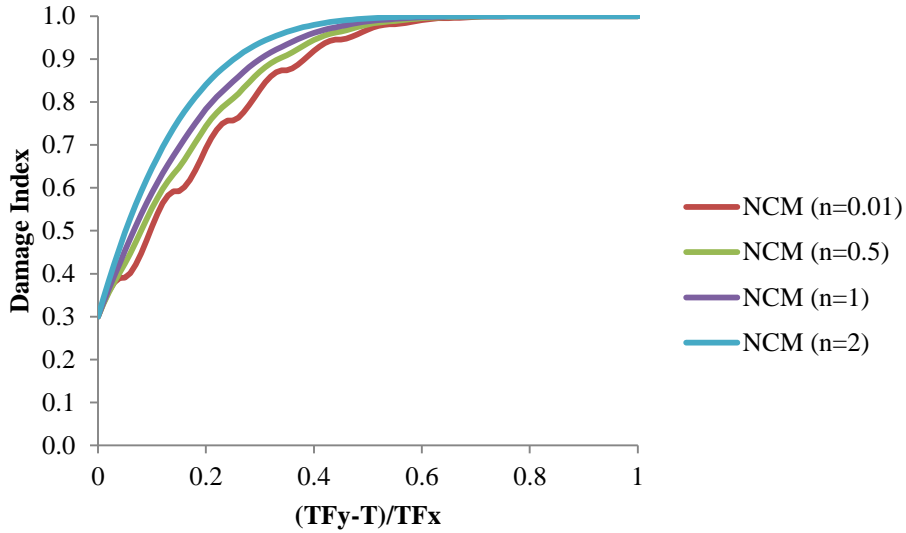


Figure 5.8 Sensitivity of NCM to time of flight and wave attenuation

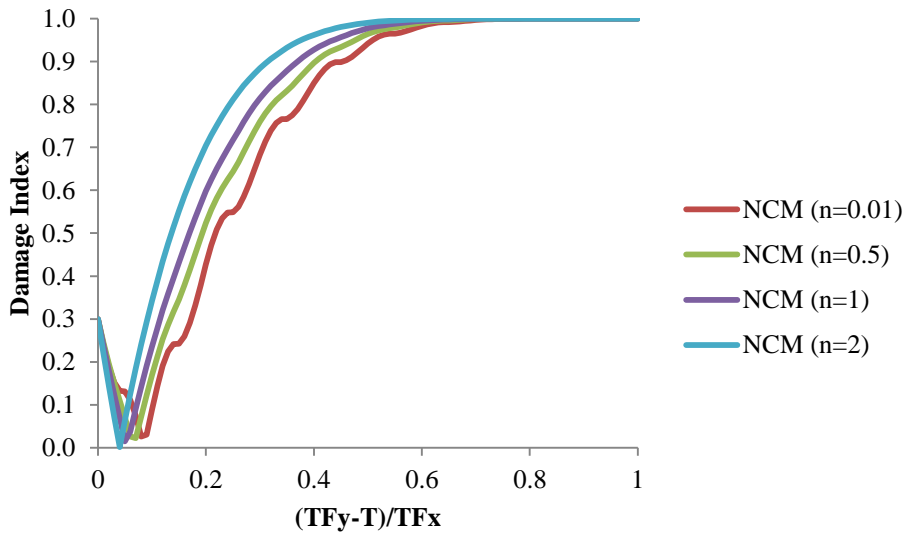


Figure 5.9 Sensitivity of NCM to time of flight and wave amplitude increase

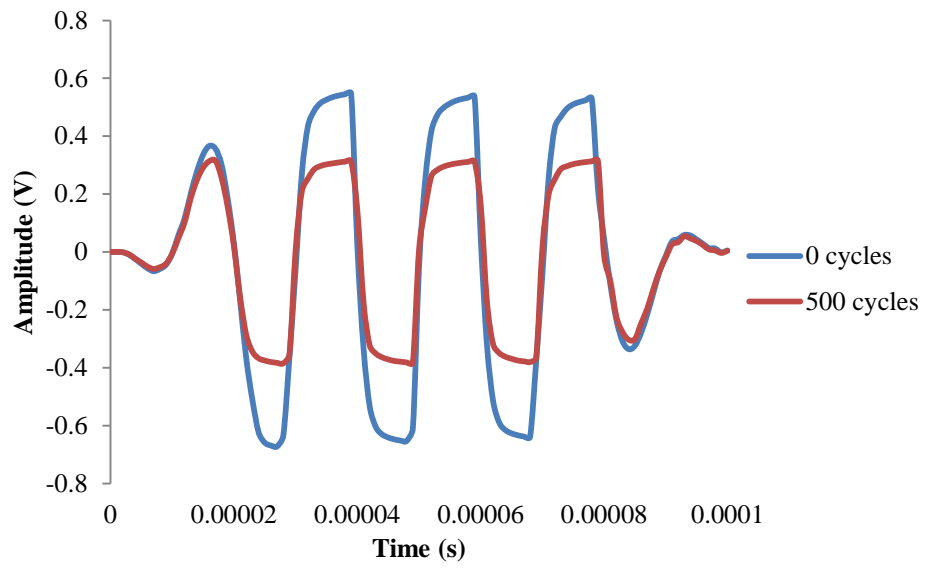


Figure 5.10 Received signals at 0 cycles and 500 cycles in the experiment

## CHAPTER 6

### CONCLUSIONS AND FUTURE WORK

#### 6.1 Conclusions

A well-established structural health monitoring (SHM) technique, the Lamb wave based approach, offers improvements in safety and enormous economic benefits over maintenance based on an estimated time for repair. Therefore, it is important to establish a system for damage detection especially for large structures for effective condition based maintenance. In this study, SHM was used for fatigue damage identification in a laminated composite. Intact (baseline) specimens and specimens having 50.8 *mm* (2 *inch*) length built-in delamination were fabricated using hand layup followed by compression molding of the laminate at elevated temperature. PZT actuators and sensors were used to actuate Lamb waves and receive propagated waves in composite specimens. National Instruments LabVIEW software was used to synchronize the actuation and response measurement, and measure loads and displacements during fatigue tests. Fatigue cycling under three-point bending was conducted and delamination growth was observed by taking high-resolution photographs every 500 cycles until specimens failed. SDC and NCM damage indices were used for evaluating fatigue damage. Finite elements models were used to test the validity of SDC and NCM for detecting fatigue damage, and the FE results were compared with the experimental data.

The limited experiment and simulation results showed that the SDC damage index was almost constant before specimens fractured while trend lines of NCM were increasing for fatigue delamination-related damage identification in composites. Thus, NCM may identify

delamination growth under fatigue loading but further research is necessary to confirm this conclusion, taking account of the disadvantages of NCM discussed in the section 5.2. When time of flight and wave increase simultaneously occur, NCM tends to oscillate and bending of a specimen affects results in NCM.

Validity of both damage indices, SDC and NCM, for fatigue damage was discussed in this thesis. Both damage indices do not linearly increase to the damage growth. Thus, a careful selection of a feature extraction from waveforms is necessary. This information can be used for future work.

## **6.2 Future work**

A high frequency Lamb wave, more than 200 kHz, is preferred for SHM to avoid interference with flexural modes and detect smaller size of damage. However, Lamb wave with a high frequency will generate multiple modes, which make a received signal complicated. A careful selection of Lamb wave frequency is required.

Array of sensors and a correlation analysis based algorithm called RAPID will carry much better information for detecting damage, location of damage, and severity of damage [42].

A different actuator or sensor such as FBG and MFC may show improved performance in SHM. They can be embedded in a structure because both are small and light weight. In addition, MFC can be used for the combination of a damage sensing and a self-healing system because it is mechanically flexible and can be heated up as shown in Figure 6.1. SHM is able to identify damage but a highly desirable attribute for a next generation composite material is to autonomously heal the damage. The self-healing system is composed of carbon fibers with a mendable polymer matrix, thermoplastic poly (ethylene-co-methacrylic acid, EMAA), which is

activated by heat [43]. MFC can be used for a self-healing process along with SHM, which is able to prevent catastrophic damage in a structure.

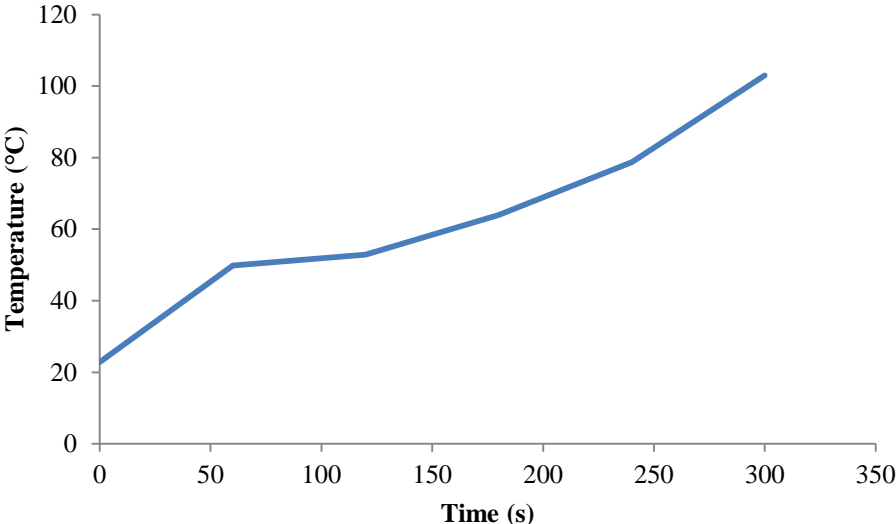


Figure 6.1 Temperature increase of MFC

## REFERENCES

- [1] D. Rosato, "Advanced in the art and science of metal to plastic replacement," 2009.
- [2] Y. Aoki, H. Suemasu and T. Ishikawa, "Damage propagation in CFRP laminates subjected to low velocity impact and static indentation," *Advanced Composite Materials* 16.1, pp. 45-61, 2007.
- [3] "Accident Common Themes," Federal Aviation Administration, [Online]. Available: [http://lessonslearned.faa.gov/ll\\_main.cfm?TabID=4&LLID=16&LLTypeID=2#null](http://lessonslearned.faa.gov/ll_main.cfm?TabID=4&LLID=16&LLTypeID=2#null). [Accessed 7 May 2015].
- [4] C. Harris, "World History Project," World History Project Team, [Online]. Available: <http://worldhistoryproject.org/1994/10/21/seongsu-bridge-collapse>. [Accessed 7 May 2015].
- [5] Z. Su and L. Ye, Identification of damage using lamb wave, 2009.
- [6] Y. Fujino and D. M. Siringoringo, "Structural health monitoring of bridge in Japan: an overview of the current trend," in *Fourth International Conference on FRP Composites in Civil Engineering (CICE2008)*, Zurich, Switzerland, 2008.
- [7] "Airplane Health Management: Monitoring the Airplane in Flight," Boeing, 30 July 2013. [Online]. Available: <http://www.boeing.com/features/2013/07/bca-airplane-health-mgmt-07-30-13.page>. [Accessed 8 May 2015].
- [8] H. Sohn, C. R. Farrar, F. Hemez, D. D. Shunk, D. W. Stinemat, B. R. Nadler and J. J. Czamecki, "A Review of Structural Health Monitoring Literature: 1996-2001," 2004.
- [9] W. J. Staszewski, S. Mahzan and R. Traynor, "Health monitoring of aerospace composite structures-Active and passive approach," *Composite Science and Technology*, vol. 69, no. 11-12, pp. 1678-1685, 2009.
- [10] S. S. Kessler, S. M. Spearing and C. Soutis, "Damage detection in composite materials using Lamb wave methods," *Smart Materials and Structures*, vol. 11, pp. 269-278, 2002.
- [11] S. S. Kessler, S. M. Spearing, M. J. Atalla, C. E. Cesnik and C. Soutis, "Structural health monitoring in composite," *Smart Structure and Material*, 2001.
- [12] A. Nagabhushana, M. Spiegel, S. Adu, N. Hayes, D. Paul, K. Trivedi, B. Fairbee, H. Zheng,

- A. Gerrity, S. Kotru, S. Roy, M. Barkey and S. Burkett, "Numerical analysis for structural health monitoring of a damaged composite panel using PZT actuators and sensors," in *Smart Structures and Material-None destructive evaluation and health monitoring*, San Diego, CA, United States, 2012.
- [13] H. Gao, Y. Shi and J. L. Rose, "Guided Wave Tomography on an Aircraft Wing with Leave in Place," in *AIP*, 2005.
- [14] S. Torkamani, S. Roy, M. E. Barkey, E. Sazonov, S. Burkett and S. Kotru, "A novel damage index for damage identification using guided waves with application in laminated composites," *Smart Materials and Structures*, vol. 23, no. 9, 2014.
- [15] H. Lamb, "On waves in an elastic plate," *Proceedings of the Royal Society of London. Series A, Containing Papers of a Mathematical and Physical Character*, vol. 93, pp. 114-128, 1917.
- [16] D. Worlton, "Experimental Confirmation of Lamb Waves at Megacycle Frequencies," *Journal of Applied Physics*, vol. 32, pp. 967-971, 1961.
- [17] Ş. Sorohan, N. Constantin, M. Găvan and V. Anghel, "Extraction of dispersion curves for waves propagating in free complex waveguides by standard finite element codes," *Ultrasonics*, vol. 51, no. 4, pp. 503-515, 2011.
- [18] A. H. Nayfeh, *Wave propagation in layered anisotropic media*, Elsevier, 1995.
- [19] L. Knopoff, "A matrix method for elastic wave problem," *Bulletin of the Seismological Society of America*, vol. 54, pp. 431-438, 1964.
- [20] I. Bartoil, A. Marzani, F. L. Scalea and E. Viola, "Modeling wave propagation in damped waveguides of arbitrary cross-section," *Sound and Vibration*, vol. 295, no. 3-5, pp. 685-707, 2006.
- [21] P. P. Delsanto, R. S. Schechter and R. B. Mignogna, "Connection machine simulation of ultrasonic wave propagation in materials III: The three-dimensional case," *Wave Motion*, vol. 26, no. 4, pp. 329-339, 1997.
- [22] T. Monnier, "Lamb wave-based impact damage monitoring of a stiffened aircraft panel using piezoelectric transducers," *Intelligent Material Systems and Structures*, vol. 17, pp. 411-421, 2006.
- [23] A. k. Abdelrahman, "Ultrasonics transduction in metallic and composite structures for structural health monitoring using extensional and shear horizontal piezoelectric wafer active sensors," Ph.D. dissertation, University of South Carolina, Columbia, 2014.

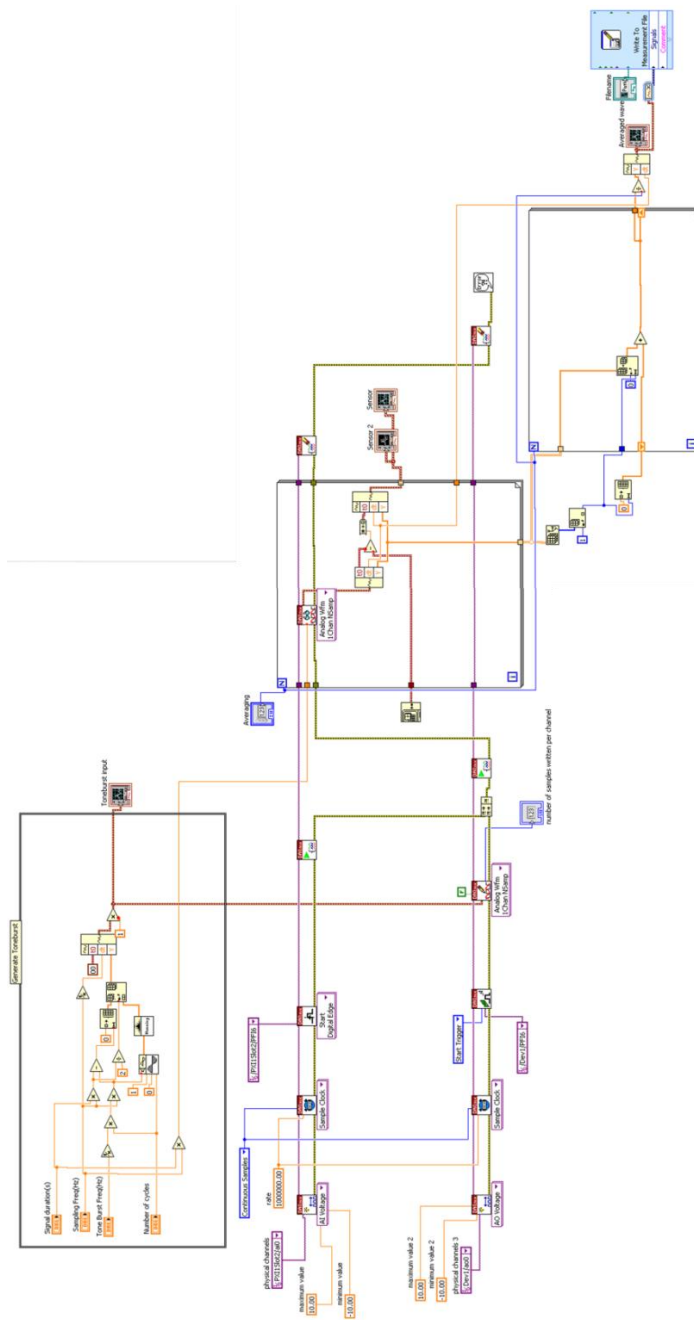
- [24] P. Bocchini, A. M. A. Marzani and E. Viola, "Graphical user interface for guided acoustic waves," *Computing in Civil Engineering*, vol. 25, no. 3, pp. 202-210, 2011.
- [25] K. Diamanti and C. Soutis, "Structural health monitoring techniques for aircraft composite structures," *Progress in Aerospace Sciences*, vol. 46, pp. 342-352, 2010.
- [26] D. Adams, *Health monitoring of structural materials and components: Methods with application*, John Wiley & Sons, 2007.
- [27] X. Zhao, H. Gao, G. Zhang, B. Ayhan, F. Yan, C. Kwan and J. L. Rose, "Active health monitoring of an aircraft wing with embedded piezoelectric sensor/actuator network: I. Defect detection, localization and growth monitoring," *Smart Materials And Structures*, vol. 16, pp. 1208-1217, 2007.
- [28] F. Yan, R. L. Royer JR and J. L. Rose, "Ultrasonic guided wave imaging techniques in structural health monitoring," *Intelligent Material Systems and Structures*, vol. 21, pp. 377-384, 2010.
- [29] C. J. Lissenden, F. Yan, E. Hauck, D. M. Noga and J. L. Rose, "Internal damage detection in a laminated composite plate using ultrasonic guided waves," in *American Institute of Physics*, Portland, Oregon, USA, 2007.
- [30] C. Keulen, M. Yildiz and A. Suleman, "Damage detection of composite plates by lamb wave ultrasonic tomography with a sparse hexagonal network using damage progression trends," *Shock and Vibration*, vol. 2014, 2014.
- [31] Z. Su, X. Wang, Z. Chen, L. Ye and D. Wang, "A built-in active sensor network for health monitoring of composite structures," *Smart Materials And Structures*, vol. 15, pp. 1939-1949, 2006.
- [32] S. Takeda, Y. Aoki, T. Ishikawa, N. Takeda and H. Kikukawa, "Structural health monitoring of composite wing structure during durability test," *Composite Structures*, vol. 79, no. 1, pp. 133-139, 2007.
- [33] J.-B. Ihn and F.-K. Chang, "Detection and monitoring of hidden fatigue crack growth using a built-in piezoelectric sensor/actuator network: I. Diagnostics," *Smart materials And Structures*, vol. 13, pp. 609-620, 2004.
- [34] A. El-Kafrawy, "Crack detection by modal analysis in 3D beams based on FEM," *International Journal of Mechanics and Materials in Design*, vol. 7, pp. 265-282, 2011.
- [35] Ș. Sorohan, N. Constantin, M. GĂVAN and V. Anghel, "Numerical extraction of dispersion curves used in lamb wave inspections," in *SISOM*, Bucharest, 2006.

- [36] V. Giurgiutiu, J. Bao and W. Zhao, "Active sensor wave propagation health monitoring of beam and plate structures," in *Proceedings of the SPIE's 8th International Symposium on Smart Structures and Materials*, Newport Beach, CA, 2001.
- [37] S. H. Di'az Valde's and S. Costas, "Real-time nondestructive evaluation of fiber composite laminates using low-frequency Lamb wave," *Acoustic Society of America*, vol. 36, no. 2, pp. 2026-2033, 2002.
- [38] S. S. Kessler, S. M. Spearing and C. Soutis, "Structural health monitoring in composite materials using lamb wave methods," *Smart Material and Structure*, vol. 11, pp. 269-278, 2001.
- [39] R. Courant, K. Friedrichs and H. Lewy, *Über die partiellen differenzgleichungen der mathematischen physik*, Springer-Verlag, 1928.
- [40] J. T. Wang, R. W. Ross, G. L. Huang and F. G. Yuan, "Simulation of detecting damage in composite stiffened panel using lamb waves," in *American Society for Composites*, Dayton, OH, USA, 2013.
- [41] N. F. Knight, "User-defined material model for progressive failure analysis," NASA, 2006.
- [42] W. Quang and X. Jing, "Lamb wave tomography technique for crack damage detection," in *Chinese control conference*, Nanjing, 2014.
- [43] S. Meure, D. Y. Wu and S. Furman, "Polyethylene-co-methacrylic acid healing agents for mendable," *Acta Materialia*, vol. 57, no. 14, pp. 4312-4320, 2009.
- [44] J. Rose, "A baseline and vision of ultrasonic guided wave inspection potential.," *Pressur Vessel Technology*, pp. 273-284, 2002.
- [45] J. B. Ihn, "Pitch-catch active sensing methods in structural health monitoring for aircraft structures," *Structural health Monitoring*, vol. 7, pp. 5-19, 2008.
- [46] B. C. Lee and W. J. Staszewski, "Modelling of Lamb waves for damage detection in metallic structures: Part II. Wave interactions with damage," *smart materials and structures*, vol. 12, pp. 815-824, 2003.
- [47] A. Raghavan and C. E. S. Cesnik, "Review of guided-wave structural health monitoring," *The Shock and Vibration Digest*, pp. 91-114, 2007.
- [48] Z. Su, L. Ye and Y. Lu, "Guided lamb waves for identification of damage in composite structures: A review," *sound and vibration*, vol. 295, pp. 753-780, 2006.
- [49] V. Yantchev and I. Katardjiev, "Thin film Lamb wave resonators in frequency control and

- sensing applications: a review," *Journal of Micromechanics and Microengineering*, vol. 23, pp. 960-1317, 2013.
- [50] D. N. Alleyne and P. Cawley, "Optimization of lamb wave inspection techniques," *NDT&E International*, vol. 25, pp. 11-22, 1992.
- [51] P. Cawley and D. Alleyne, "The use of lamb waves for the long range inspection of large structures," *Ultrasonics*, vol. 34, pp. 287-290, 1996.
- [52] J. L. Rose, *Ultrasonic waves in solid media*, Cambridge University Press, 1999.
- [53] V. Giurgiutiu and G. Santoni, "Structural health monitoring of composite structures with piezoelectric-wafer active sensors," *AIAA Journal*, vol. 43, no. 3, pp. 565-581, 2011.
- [54] A. Raghavan and C. E. Cesnik, "Review of guided-wave structural health monitoring," *The Shock and Vibration Digest*, vol. 39, pp. 91-114, 2007.
- [55] D. E. Chimenti, "Guided waves in plates and their use in materials characterization," *Applied Mechanics Reviews*, vol. 50, pp. 247-284, 1997.

## APPENDIX A: LabVIEW program

LabVIEW program developed to do structural health monitoring.





**APPENDIX B: MATLAB program**  
MATLAB program developed to calculate NCM and SDC.

```
clc
close
clear all

% define variables %
Ncycle = 5;% number of sinusoidal peaks that exists in the tone-burst
f = 50000;% signal frequency(Hz)
fs = 1e6;% sampling frequency
t1 = 0;% initial time(s)(ms=10^-3*s)
dt = 1e-6;% dt in the experimental raw data
t2 = Ncycle/f;% end time t2=Ncycle*T=Ncycle/f
t = t1:dt:t2;
N = length(t);

%% Calculate SDC and NCM %%
filename1 = 'Ave-trigger-0-B1-f=50kHz-fs=1MHz-N=5.lvm';%baseline
filename2 = 'Ave-trigger-0-D2-13-f=50kHz-fs=1MHz-N=5.lvm';%comparison waveform

fileID1 = fopen(filename1,'r');
fileID2 = fopen(filename2,'r');

for I = 1:22
    header = fgets(fileID1);% skip header
end
for I = 1:22
    header = fgets(fileID2);% skip header
end

formatSpec = '%f %f\n';
sizeA1 = [2 Inf];
A1 = fscanf(fileID1,formatSpec,sizeA1);
A1 = A1';

formatSpec = '%f %f\n';
sizeA2 = [2 Inf];
A2 = fscanf(fileID2,formatSpec,sizeA2);
A2 = A2';
```

```

tau = A1(:,1);
M = 101;

for I = 50001:50101
    a12(I-50000,1) = A1(I,2);
end

a12 = a12(:,1)-mean(a12(:,1));
a12n = a12/max(abs(a12));
n = [0.01 0.5 1 2]'; % order of the statistical moment
rxx = xcorr(a12); % auto-correlation

SDC = zeros(2,2,Numfiles);
SDCdash = zeros(1,Numfiles);
NCM = zeros(4,Numfiles);

for I = 50001:50101
    a22(I-50000,1) = A2(I,2);
end

a22 = a22(:,1)-mean(a22(:,1));
a22n = a22/max(abs(a22));
rxy = xcorr(a12,a22); % cross-correlation

plot(1:101,a12,1:101,a22)
legend('baseline','comparison wave')

for I = 1 : (length(rxy)-1)/2+1
    rxy_a(I,1) = rxy((length(rxy)-1)/2+I,1);
    rxx_a(I,1) = rxx((length(rxy)-1)/2+I,1);
end

SDC(:, :, 1) = 1-abs(cov(a12n,a22n))/(std(a12n,0,1)*std(a22n,0,1));
SDCdash(1,1) = SDC(2,1,1);

for I = 1:4
    NCM(I,1) = abs(sum((tau(1:M,1).^n(I,1)).*abs(rxy_a(1:M,1)))-
sum((tau(1:M,1).^n(I,1)).*abs(rxx_a(1:M,1))))/sum((tau(1:M,1).^n(I,1)).*abs(rxx_a(1:M,1)));
end

fclose(fileID1);
fclose(fileID2);

```

MATLAB program developed to calculate the sensitivity of NCM and SDC to the time of flight.

```
clc
close
clear all

% define variables %
Ncycle = 5;% number of sinusoidal peaks that exists in the tone-burst
f = 50000;% signal frequency(Hz)
fs = 1e6;% sampling frequency
t1 = 0;% initial time(s)(ms=10^-3*s)
t2 = Ncycle/f;% end time t2=Ncycle*T=Ncycle/f
t = t1:1/fs:t2;% time duration having tone burst
T = t1:1/fs:2*t2;% total time duration
N = length(t);
Win = window(@hann,N); % hanning window
Toneburst = zeros(1,length(t));

% plot baseline ToneBurst %
Toneburst = 1.*Win'.*sin(2*pi*f.*t);
Zeros = zeros(1,N-1);
Toneburst = [Toneburst,Zeros];

figure
plot(T,Toneburst)
xlabel('time(s)')
ylabel('signal')

% make shifted tone burst
for I = 1:100
    Toneburstdash(:,I) = circshift(Toneburst',I);
end

Toneburstdash2 = [Toneburst ; Toneburstdash'];
Toneburstdash2 = 1*Toneburstdash2;

% calculating NCM %
tau = T';
X = Toneburst';
for I = 1:101
    Y(I,:) = Toneburstdash2(I,:);
end
Y = Y';
```

```

for I = 1:101
    rxy(:,I) = xcorr(X,Y(:,I));% cross-correlation
end

rxx = xcorr(X);% auto-correlation
M = length(tau);
n = [0.01 0.5 1 2];% order of the statistical moment
NCM = zeros(101,4);
for J = 1:4
    for I = 1:101
        NCM(I,J) = abs(sum((tau(1:M,1).^n(J,1)).*abs(rxy(M:2*M-1,I))-
sum((tau(1:M,1).^n(J,1)).*abs(rxx(M:2*M-1,1))))/sum((tau(1:M,1).^n(J,1)).*abs(rxx(M:2*M-
1,1)))));
    end
end

% Calculating SDC%
for I = 1:101
    SDC(:,I) = 1- abs(cov(X(:,1),Y(:,I)))/(std(X(:,1),0,1)*std(Y(:,I),0,1));
    SDCdash(I,1) = SDC(2,1,I);
end

figure
plot(SDCdash)

I = (1:101);
plot(I,SDCdash,I,NCM)
legend('SDC','NCM n=0.01','NCM n=0.05','NCM n=1','NCM n=2')
ylabel('Damage Index')

```

MATLAB program developed to calculate the sensitivity of NCM and SDC to the wave attenuation and increase.

```
clc
close
clear all

% define variables %
Ncycle = 5;% number of sinusoidal peaks that exists in the tone-burst
f = 50000;% signal frequency(Hz)
fs = 1e6;% sampling frequency
t1 = 0;% initial time(s)(ms=10^-3*s)
t2 = Ncycle/f;% end time t2=Ncycle*T=Ncycle/f
t = t1:1/fs:t2;% time duration having tone burst
N = length(t);
Win = window(@hann,N); % hanning window
Toneburst = zeros(1,length(t));

% plot baseline ToneBurst %
Toneburst = 1.*Win'.*sin(2*pi*f.*t);

figure
plot(t,Toneburst)
xlabel('time(s)')
ylabel('signal')

% attenuate/increase tone burst %
Factor = 0:0.1:2;
for I = 1:length(Factor)
    Toneburstdash(:,I) = Factor(I).*Toneburst';
end

Toneburstdash = Toneburstdash';

% calculating NCM %
tau = t';
a12 = Toneburst';
for I = 1:length(Factor)
    a22(I,:) = Toneburstdash(I,:);
end
a22 = a22';

for I = 1:length(Factor)
    rxy(:,I) = xcorr(a12,a22(:,I));% cross-correlation
end
```

```

rxx = xcorr(a12);% auto-correlation

% arrange cross correlation starting from the center(t=0) to the end
for J = 1 : length(Factor)
    for I = 1 : (length(rxy)-1)/2+1
        rxy_a(I,J) = rxy((length(rxy)-1)/2+I,J);
        rxx_a(I,1) = rxx((length(rxy)-1)/2+I,1);
    end
end
n = [0.01 0.5 1 2]';% order of the statistical moment
NCM = zeros(11,1);
M = length(tau);
for J = 1:4
    for I = 1:length(Factor)
        NCM(I,J) = abs(sum((tau(1:M,1).^n(J,1)).*abs(rxy_a(1:M,I))-
sum((tau(1:M,1).^n(J,1)).*abs(rxx_a(1:M,1))))/sum((tau(1:M,1).^n(J,1)).*abs(rxx_a(1:M,1))));
    end
end

figure
plot(abs(NCM))

% SDC%
for I = 1:length(Factor)
    SDC(:,I) = 1- abs(cov(a12(:,1),a22(:,I)))/(std(a12(:,1),0,1)*std(a22(:,I),0,1));
    SDCdash(I,1) = SDC(2,1,I);
end

figure
plot(SDCdash)

plot(Factor,SDCdash,Factor,NCM)
legend('SDC','NCM')
xlabel('Ay/Ax')
ylabel('Damage Index')

```